UNIVERSITÀ DEGLI STUDI DI TRIESTE

DEGLI STUDI DI TRIESTE

XXXV CICLO DEL DOTTORATO DI RICERCA IN

SCIENZE DELLA, TERRA, FLUIDODINAMICA E MATEMATICA.

INTERAZIONI E METODICHE

ADVANCED EMPIRICAL DATA ANALYSIS AND NUMERICAL SIMULATIONS FOR STRUCTURE AND SOIL DYNAMIC BEHAVIOR AS CONTRIBUTIONS TO SEISMIC RISK ASSESSMENT

Settore scientifico-disciplinare: **GEO/10**

DOTTORANDO:

MELESE TEMESGEN SALILIH

COORDINATORE:

PROF. STEFANO MASET

SUPERVISORE DI TESI:

PROF. STEFANO PAROLAI

CO-SUPERVISORE DI TES:

DR. VALERIO POGGI

ANNO ACCADEMICO 2021/2022

Acknowledgment

I am deeply indebted to my supervisor, Prof. Stefano Parolai, for giving me the opportunity to work on my PhD project and for giving me his time to comment, guide, and and follow the progress of this work. I have benefited immensely from his help, advice, and encouragement throughout my studies. I would like to thank the National Institute for Oceanography and Experimental Physics - OGS for funding this Ph.D. project. I would like to thank research group at the Seismological Research Center - CRS for their technical help and encouragement.

I would also like to thank my co-supervisor Dr. Valerio Poggi for his continuous technical support, especially in familiarizing me with the codes I worked with, and for his valuable comments and encouragement. I would like to express my special thanks to Dr. Bojana Petrovic, who helped me to access programs and data. I am grateful to my colleagues Ilaria Dreossi, AnnaMaria Sklodowska, and Elisa Venturini for their constant encouragement throughout my studies.

Abstract

Separate estimation of the attenuation due to intrinsic absorption and scattering in near-surface geology and built-in structures is essential in engineering seismology. Knowledge of the intrinsic absorption and scattering attenuation parameters could be used for site response studies; and prediction of strong motions in engineering seismology for seismic hazard and risk studies. In this study, two methods were used in this study to estimate the intrinsic and scattering attenuation parameters: the coda method to estimate the coda quality factor for the uniform half-space model and the Multi-Lapse Time Window Analysis (MLTWA) to separately estimate the intrinsic (Q_i^{-1}) and scattering (Q_{sc}^{-1}) attenuation for the uniform half-space model for a more realistic depth-dependent earth media model.

MLTWA is a method for estimating the attenuation due to intrinsic absorption and scattering separately. It compares the seismic energy integrated from three consecutive seismogram windows starting from the S-wave arrival time and plotted against hypocentral distance. In this study, the MLTWA method is modified to use a vertical array of seismograms to separately estimate the scattering and intrinsic seismic attenuation. To overcome the problem of intensive computational requirements associated with the application of MLTWA to the multi-layer earth model, a simulated annealing inversion strategy is developed. The parameter space is constrained using grid search to our search domain of those with a potential solution. This parameter space is used in simulated annealing to rapidly converge to the solution in a few hundred iterations or less.

Seismic data collected from a vertical array of seismic sensors installed in a borehole and a nearby building test site in Atakoy, Istanbul, Turkey are used to estimate the attenuation parameters of the building and the subsurface beneath it.

Intrinsic and scattering attenuation parameters are estimated for a building and two layers below the building. Frequency dependent shear wave attenuation values Q_i, Q_{sc}, and Q_s are estimated for the frequency range from 1 to 15 Hz. Qs values of $Q_s = 2f^{1.25}$, $Q_s = 2f^{1.75}$ and $Q_s = 20f^{1.0}$ are estimated for the building, the first layer, and the half-space below, respectively. It is generally observed that the scattering attenuation dominates over the intrinsic absorption. The results of this study are in agreement with to a previous study on the same site by Parolai et al. (2010). He estimated Qs values of 30, 46, and 99 for the 0-50, 0-70, and 0-140 m depth ranges, respectively, using spectral fitting for the 1 to 15 Hz frequency band. This study estimates Qs values of 16, 23, and 83 for the 45 m high building, the 50 m thick shallow layer, and the half space below at 5 Hz, respectively, which are comparable to the previous study

Keywords: Seismic coda, Intrinsic absorption, Scattering, MultiLapse Time Window analysis (MLTWA), Simulated annealing, Grid search

Table of Contents

List of Figures

List of Tables

Chapter 1

Introduction

1.1 Background of the study

The propagation of the S-wave through the crust is strongly influenced by scattering loss, intrinsic absorption and geometric scattering. The energy oss due to seismic scattering determines the shape of the seismic envelope and the spatial distribution of the energy, while intrinsic absorption leads to an exponential decay of the S-wave envelope. Geometric scattering is due to the elastic wavefront that propagates with increasing distance from the source. Intrinsic and scattering attenuation patterns reveal the nature of the Earth's interior and impose constraints on seismic wave propagation. Thus, the ability to separately estimate the spatial distributions of intrinsic (Q_i^{-1}) and scattering (Q_{sc}^{-1}) attenuation is critical for improving our understanding of the Earth's structure.

Several different scattering theories have been developed to model seismic coda envelopes.Wu and Aki (1985) was the first to include multiple scattering to account for the relative contributions of scattering and intrinsic attenuation. relative contributions of scattering and intrinsic absorption to total attenuation. attenuation. Hoshiba (1991) provided the numerical basis for the method by calculating the S-wave energy density from a Monte Carlo simulation of multiple isotropic scattering.

Studies of scattering (Q_{sc}^{-1}) and intrinsic (Q_i^{-1}) attenuation, as well as total S-wave attenuation (Q_s^{-1}), have been performed worldwide (Fehler et al., 1992; Bindi et al., 2006; Sato et al., 2012). These studies are useful for inferring both the materials and the physical state of the lithosphere. Q_{sc}^{-1} reflects the presence of heterogeneities that redistribute wave energy without any loss, and Q_i^{-1} represents the anelasticity that converts seismic energy to thermal energy due to internal friction between grain particles. Several mechanisms for intrinsic attenuation as described by O'Connell and Budiansky (1977) include the resistive and viscous properties of oscillator models of atoms in crystalline lattices, the movement of interstitial fluids between grain bound-

aries and cracks, and the frictional sliding of cracks. Vargas et al. (2004) reported high values of both Q_{sc}^{-1} and Q_i^{-1} from volcanic regions, while high Q_i^{-1} was observed in region of high heat flow (Abdel-Fattah et al., 2008).

Multiple Lapse Time Window Analysis (MLTWA) is a commonly used approach for separating Q_{sc}^{-1} and Q_i^{-1} (Hoshiba, 1993; Fehler et al., 1992; Sato et al., 2012), based on the application of radiative transfer theory proposed by (Wu and Aki, 1985). MLTWA allows one to estimate the relative contributions of scattering loss (Q_{sc}^{-1}) and intrinsic absorption (Q_i^{-1}) to the total S-wave attenuation (Q_T^{-1}) of S-wave envelopes (Fehler et al., 1992); Sato et. al (2012). The MLTWA is based on the observations of (Fehler et al., 1992) that the direct S-wave, whose amplitude is controlled by the early part of the seismogram is controlled by the total attenuation of the media and the S-coda is composed entirely of scattered S-waves whose amplitudes are mainly controlled by the scattering coefficients.

Previous studies such as (Fehler et al., 1992; Bindi et al., 2006; Akinci et al., 2020) have used MLTWA to estimate attenuation for the crust and upper mantle using earthquakes recorded by multiple stations spaced tens of kilometers apart at the Earth's surface. Hoshiba (1993) proposed a method to use seismic data from a single station recording multiple earthquakes using MLTWA. In this study, we propose a new approach for estimating the scattering and intrinsic attenuation of the shallow crust using MLTWA. The new approach uses seismograms from a vertical array of seismological stations installed inside boreholes and buildings to estimate attenuation due to scattering and intrinsic absorption.

1.2 Seismic wave attenuation

Seismic wave attenuation is an intrinsic property of earth materials that causes energy dissipation as seismic waves propagate through earth materials. This phenomenon causes the amplitude of seismic waves to decrease as they propagate away from the source through the earth's medium.

The most common parameter used to measure the attenuation of seismic waves is the dimensionless parameter called **quality factor Q**, and its reciprocal Q^{-1} (attenuation). Many studies have been conducted to understand the characteristics of seismic attenuation by quality factor Q. It measures the relative loss of energy per vibration cycle.

$$Q = \frac{2\pi E}{\Delta E} \tag{1.1}$$

E and ΔE are the energy of seismic waves and energy lost during a wave cycle, respectively. Q increases with the density and velocity of a material. The reciprocal of the quality factor Q (Q^{-1} is sometimes called the attenuation or internal friction

(Knopoff and Hudson, 1964), and is related to the strength of attenuation..

When Q is frequency independent, i.e., each frequency loses the same amount of energy per cycle.

$$Q = Q_0.f^{\alpha} \tag{1.2}$$

where Q is the quality factor for each phase (P and S wave). Each mode has its own amplitude decay rate, so the attenuation factor Q must be calculated for each mode. Different values of Q result from the way each mode samples the ground.

When an earthquake occurs, some of the seismic energy released is dissipated in the form of heat generated by friction as the rock masses slide along the fault surface. The remaining energy is dissipated partly as work, resulting in the displacement of masses and partly in the form of seismic waves. Therefore, the following three phenomena are the main causes of seismic wave attenuation: geometric propagation, intrinsic absorption, and seismic scattering.

1.2.1 Geometrical spreading

Geometric spreading decreases the energy density as an elastic wave-front expands with increasing distance from its source, as shown in figure 1.1. Seismic energy radiates as a wave-front from a point source to be distributed over a spherical surface of increasing size. As the wave-front travels away from the source, the initial energy released by the seismic source is distributed over an increasing volume. Therefore, the amplitude of the seismic wave decreases with distance from the source.

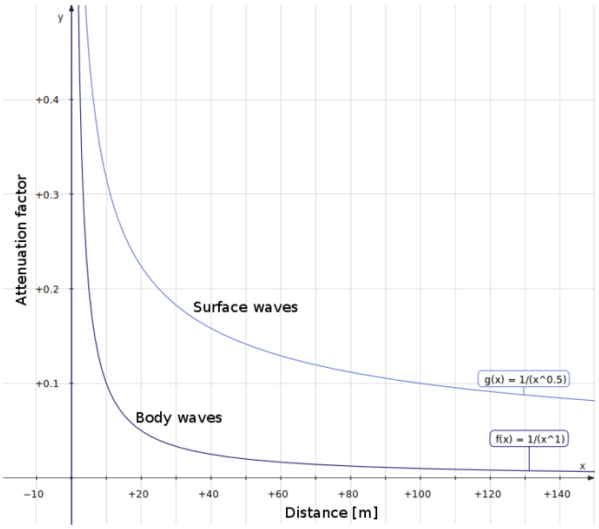

Figure 1.1: Geometrical decay (Lore.trango, 2010)

In a homogeneous Earth of constant velocity and density, the amplitude of body

waves decays proportional to the reciprocal of the distance between the source and receiver ($\frac{1}{r}$). The energy density of seismic waves is proportional to $\frac{1}{r^2}$, where r is the radius of the wave-front.

1.2.2 Seismic scattering

The modification of seismic waves caused by the three-dimensional heterogeneities is generally referred to as seismic wave scattering. Scattering attenuation occurs when elastic energy is scattered and redistributed in directions away from the receiver or in waves arriving at the receiver in later time windows. Scattering occurs by Reflection, refraction, and mode conversion of elastic energy by wavelength-scale irregularities in the medium. In the presence of obstacles or lateral variations of elastic parameters, wave-fronts are distorted, and seismic energy can be deflected in all possible directions .

Scattering is an important phenomenon caused by the heterogeneity of the Earth's crust and mantle. Scattering of high-frequency seismic waves reveals the presence of small-scale heterogeneity in the lithosphere. Since the scatterers are assumed to be randomly distributed, the scattered waves are inherently incoherent and their phase can be neglected. Therefore, the scattered wave power is the sum of the individual scattered waves from all the heterogeneity. A hypothetical diagram is shown in Figure 1.2 to illustrate the scattering process of an incident seismic wave through a heterogeneous medium.

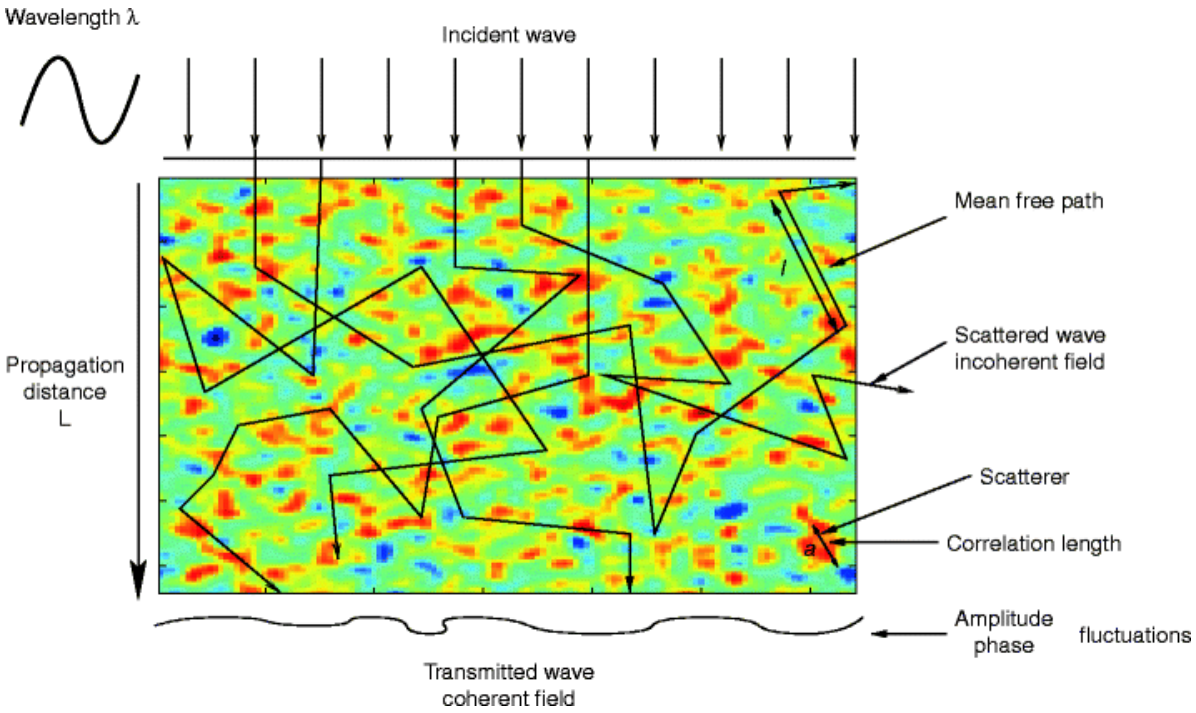

Figure 1.2: Illustration of seismic scattering by Ludovic Margerin in Encyclopedia of Solid Earth Geophysics (2011)

The Earth's crust contains a wide variety of rock types, with grain sizes ranging from a few millimeters to many kilometers. Small-scale heterogeneities in the crust are revealed by the scattered high-frequency components of seismic waves. The discontinuity in the crust is contributed by tectonic faulting and folding processes and large-scale crustal movements associated with plate tectonics. Distributed cracks and cavities also cause heterogeneity in the crust (Kikuchi, 1981).

The Earth is laterally heterogeneous everywhere, from the crust and mantle to the core, with scales ranging from the grain size of rocks to the lowest orders of global spherical harmonics. Heterogeneities with different scales have different effects on seismic waves. The velocity and density heterogeneities can cause changes in the waveform, phase (or travel time), amplitude variations, and apparent attenuation of the direct arrivals. They can also generate coda waves such as the P-coda, S-coda, and Lg-coda caused by lithospheric heterogeneities.

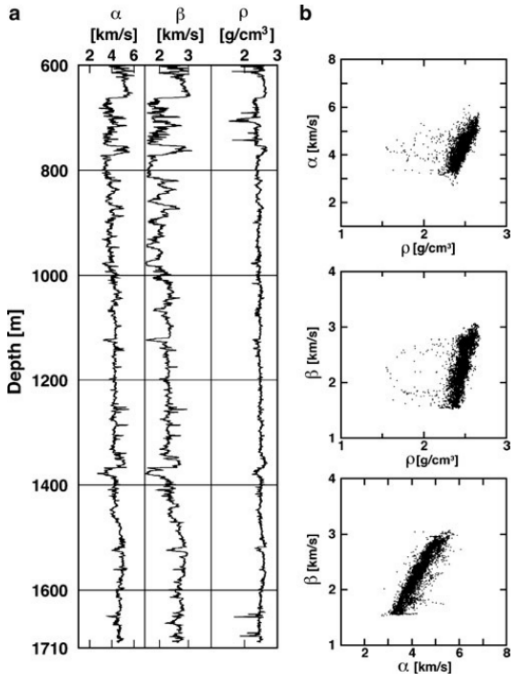

Figure 1.3: (a) Well-logs showing P- and S-wave velocities and mass density vs. depth for well YT2 in Kyushu, Japan. (b) Scattergrams showing correlation among the physical properties measured at the same depth. The figure is adopted from Shiomi et al. (1997).

The heterogeneity is stronger in the near-surface part of the crust, and its direct evidence for random inhomogeneities in the shallow crust can be seen in log data from boreholes as shown in the figure 1.3. The velocity of seismic waves generally increases with increasing depth in the Earth; However, there is considerable spatial variation of velocity is evident in the logs. This increase in the velocity of the medium from the surface down also affects the seismic wave's amplitude of the seismic waves recorded in boreholes. It is observed that the amplitude of the seismograms increases as the seismic wave propagates vertically upward toward the surface in borehole sensors. This is due to the decreasing impedance from depth to the surface.

The scattered seismic wave strongly depends on the size of the heterogeneity. For heterogeneities of scale "a" and strength (perturbation index ν), the seismic wave propagation regime can be characterized by three dimensionless numbers: $ka = \frac{2\pi a}{\lambda}$, L/a and ν where k is the wave number and λ is the wavelength in the medium, L is the propagation length or the extent of the heterogeneous region. If $ka \ll 1$ or $ka \gg 1$, the waves are not affected by the obstacle, and the medium behaves like a homogeneous body. Seismic scattering increases as the wavelength approaches to the size of the heterogeneities. Figure 1.4 summarizes the scattering strength of the Earth's medium at different scales.

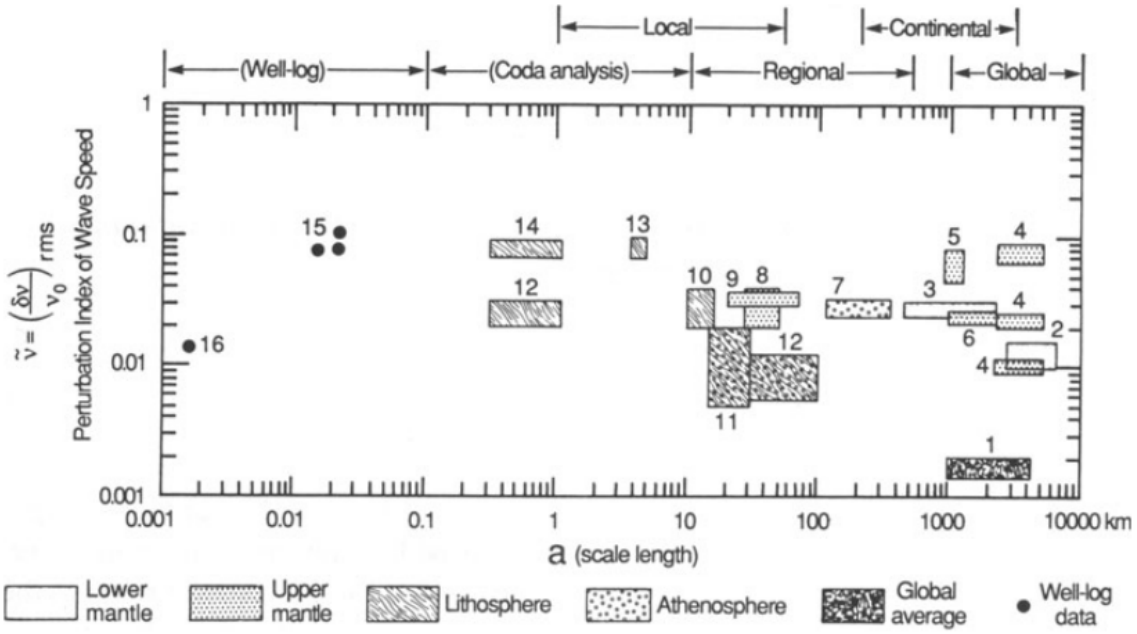

Figure 1.4: Strength-scale distribution of heterogeneities in the earth (Wu and Aki, 1988)

1.2.3 Intrinsic attenuation

Intrinsic attenuation describes the loss of energy to heat or other forms of energy due to anelasticity of the medium. Attenuation mechanisms are based on the observation that crustal rocks have microscopic cracks and pores that may contain fluids. In an elastic medium, mechanical energy is extracted from each passing wave and converted to another form, such as heat. This occurs through shear wave motion associated with lateral motion of the lattice, movement of interstitial fluids between grain boundaries and cracks (O'Connell and Budiansky, 1977), frictional sliding of cracks, and changes in viscosity. Therefore, a softer medium or the presence of water in the pores of the rock will increase the amount of energy lost as heat as the wave passes through it. This process is called absorption, and is irreversible.

Absorption is related to the frequency of the seismic waves. In general, the higher the frequency, the greater the absorption. This transformation results in a decrease in amplitude and a broadening of the pulse. This phenomenon is called the low-pass filter effect. As the wave spreads, the attenuation removes the high frequency component of the pulse.

Intrinsic attenuation of seismic waves is modeled by a harmonic oscillator composed of a spring and a dash-pot. $F = ma$, is used to describe the displacement $u(t)$ of the mass m.

$$m\frac{d^2u(t)}{dt^2} + ku(t) = 0 \tag{1.3}$$

Once set in motion by an impulse, the frictionless system has a purely elastic response described by a harmonic oscillation.

$$u(t) = Ae^{i\omega_0 t} + Be^{i\omega_0 t}, \tag{1.4}$$

The mass moves back and forth with a natural frequency.

$$\omega_0 = (\frac{k}{m})^{\frac{1}{2}} \tag{1.5}$$

One example of this general solution is

$$u(t) = A_0 cos(\omega_0 t) \tag{1.6}$$

This undamped oscillation continues forever once the motion is started because no energy is lost. For a spring-mass system with a dashpot. The damping force is proportional to the velocity of the mass and opposes its motion. Therefore, the equation of motion becomes

$$m\frac{d^2u(t)}{dt^2} + \gamma m\frac{du(t)}{dt} + ku(t) = 0 \tag{1.7}$$

Where γ is the damping factor. For simplicity simplify, we use the quality factor.

$$Q = \frac{\omega_0}{\gamma} \tag{1.8}$$

rewriting the above equation

$$\frac{d^2u(t)}{dt^2} + \frac{\omega}{Q}\frac{du(t)}{dt} + \omega_0^2 u(t) = 0 \tag{1.9}$$

The solution is based on the fact that the displacement is the real part of the complex exponential.

$$u(t) = A_0 e^{ipt}, \tag{1.10}$$

Where p is a complex parameter. Substituting eqn. 1.7 into eqn. 1.6

$$(-p^2 + \frac{ip\omega_0}{Q} + \omega_0^2)A_0 e^{ipt} = 0. \tag{1.11}$$

For this to be satisfied for all values of t,

$$(-p^2 + \frac{ip\omega_0}{Q} + \omega_0^2) = 0. \tag{1.12}$$

Breaking p into real and imaginary parts,

$$p = a + ib, p^2 = a^2 + 2iab - b^2, \tag{1.13}$$

so Eqn. 1.11 gives

$$-a^2 - 2iab + b^2 + \frac{ia\omega_0}{Q} - b\frac{\omega_0}{Q} + \omega_0^2 = 0 \tag{1.14}$$

splitting the real and imaginary

$$Real : -a^2 + b^2 - b\frac{\omega_0}{Q} + \omega_0^2 = 0, \tag{1.15}$$

$$Imaginary : -2ab + a\frac{\omega_0}{Q} = 0 \tag{1.16}$$

Solving the imaginary part for b gives

$$b = \frac{\omega_0}{2Q} \tag{1.17}$$

and inserting this into the equation for the real part gives

$$a^2 = \omega_0^2 - \frac{\omega_0^2}{4Q^2} = \omega_0^2(1 - \frac{1}{4Q^2}) \tag{1.18}$$

Thus

$$\omega_0 = a = \omega_0^2(1 - \frac{1}{4Q^2})^{\frac{1}{2}}, \tag{1.19}$$

Rewrite Eqn 1.19 with separate real and imaginary parts

$$u(t) = A_0 e^{i(\omega t + ibt)} = A_0 e^{-bt} e^{i\omega t} \tag{1.20}$$

The real part is the solution for the damped harmonic displacement,

$$u(t) = A_0 e^{-\frac{\omega t}{2Q}} cos(\omega t) \tag{1.21}$$

The exponential term expresses the decay of the envelope of the signal, or the overall amplitude as shown in the figure 1.5.

$$A(t) = A_0 e^{-\frac{\omega t}{2Q}} \tag{1.22}$$

Since the energy of the oscillating system is proportional to the square of the amplitude

$$E(t) = \frac{1}{2}kA(t)^2 = \frac{1}{2}kA_0^2 e^{-\frac{\omega t}{Q}} = E_0 e^{-\frac{\omega t}{Q}} \tag{1.23}$$

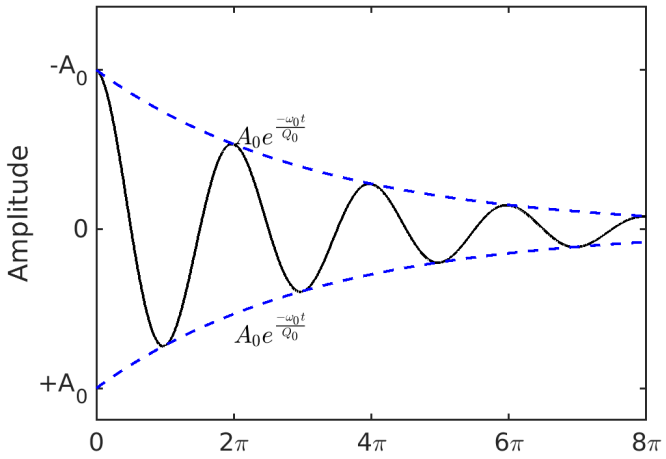

Figure 1.5: Wave amplitude for a damped harmonic oscillator

1.3 Objectives of the Study

The purpose of this study is to develop an approach using vertical seismic array to estimate the contribution of scattering and intrinsic seismic attenuation in the near-surface geology and inside buildings.

Therefore, the goal of this research is to

- Estimate the scattering and intrinsic seismic attenuation separately and their contribution to the total seismic waves attenuation.
- A better understanding of the mechanism of seismic wave attenuation by the shallow crust and buildings.
- Development of an alternative approach for estimating scattering and intrinsic seismic attenuation coefficients from vertical seismic arrays.

- Separately estimate the scattering and intrinsic quality factors of in near-surface geology and buildings.
- Estimate near-surface crustal and building attenuation parameters from seismograms recorded by a vertical array of seismic sensors installed in boreholes and buildings.

1.4 Significance of the Study

The amplitudes of earthquake ground motions at observation sites are influenced by source characteristics, propagation path, and local site conditions. The effects of propagation paths on ground motions are due to the attenuation of propagating seismic waves. Therefore, the study of seismic wave attenuation is essential for earthquake ground motion simulation and seismic hazard analysis in a region.

The study of the attenuation of the seismic wave is important because of the following reasons

- The study of the attenuation of the propagating seismic waves along the propagation path provides information about the characteristics of the medium, such as the physical properties of the material and the degree of heterogeneity of the Earth's interior.
- Knowledge of the attenuation characteristics of the medium along the source-station path provides for obtaining more reliable information about the earthquake source parameters.
- A good estimation of scattering and intrinsic attenuation will help for the prediction of strong motions in engineering seismology , which is essential for seismic hazard and risk studies.
- Knowledge of scattering and attenuation is important in the study of geothermal reservoirs. A high intrinsic attenuation could indicate that a region is saturated with a large amount of water, possibly indicating a greater porosity, which would mean more water for the geothermal plant (Hess:2013)

Chapter 2

Seismic wave propagation

2.1 Seismic wave equation

Earthquakes and other disturbances create seismic waves that provide information about the sources of the waves and the material they pass through. Seismic waves propagate through the earth because the material within it can undergo internal deformation.

The equation of motion has solutions that describe the two types of seismic (elastic) waves. These are compressional and shear waves.

The equation of motion

$$\sigma_{ij,j}(x,t) + f_i(x,t) = \rho \frac{\partial^2 u_i(x,t)}{\partial t^2} \tag{2.1}$$

These types of waves propagate at different speeds that depending on the different on the elastic properties of the material.

Let us consider a homogeneous region one of the uniform properties of the material. We assume that the region does not contain a source of seismic waves, which is required by a body force. As the waves propagate away from the source, the relationship between the stresses and displacements is given by the homogeneous equation of motion, which does not include any a body force term, so F = ma becomes

$$\sigma_{ij,j}(x,t) = \rho \frac{\partial^2 u_i(x,t)}{\partial t^2} \tag{2.2}$$

Solve the equation 2.2 in Cartesian (x, y, z) coordinate system, starting with the x component

$$\frac{\partial \sigma_{xx}(x,t)}{\partial x} + \frac{\partial \sigma_{xy}(x,t)}{\partial y} + \frac{\partial \sigma_{xz}(x,t)}{\partial z} = \rho \frac{\partial^2 u_x(x,t)}{\partial t^2} \tag{2.3}$$

To express this in terms of displacements, we use the constitutive law for an isotropic elastic medium,

$$\sigma_{ij} = \lambda \theta \delta_{ij} + 2\mu \sigma_{ij} \tag{2.4}$$

Writing the strain in terms of displacements, we get

$$\begin{aligned} \sigma_{xx} &= \lambda\theta\delta + 2\mu e_{xx} = \lambda\theta + 2\mu \frac{\partial u_x}{\partial x} \\ \sigma_{xy} &= 2\mu e_{xy} = \mu(\frac{\partial u_x}{\partial y} + \frac{\partial u_y}{\partial x}) \\ \sigma_{xz} &= +2\mu e_{xz} = \mu(\frac{\partial u_x}{\partial z} + \frac{\partial u_z}{\partial x}) \end{aligned} \tag{2.5}$$

Next, we take the derivatives of the stress components.

$$\begin{aligned} \frac{\partial \sigma_{xx}}{\partial x} &= \lambda \frac{\partial \theta}{\partial x} + 2\mu \frac{\partial^2 u_x}{\partial x^2} \\ \frac{\partial \sigma_{xy}}{\partial y} &= 2\mu(\frac{\partial^2 u_x}{\partial y^2} + \frac{\partial^2 u_y}{\partial x \partial y}) \\ \frac{\partial \sigma_{xz}}{\partial z} &= 2\mu(\frac{\partial^2 u_x}{\partial z^2} + \frac{\partial^2 u_z}{\partial x \partial z}) \end{aligned} \tag{2.6}$$

For a homogeneous material, the elastic constants do not vary with position. Substitute the derivatives into the equations of motion and use the definition of dilatation.

$$\Theta = \nabla \cdot u = \frac{\partial u_x}{\partial x} + \frac{\partial u_y}{\partial y} + \frac{\partial u_z}{\partial z} \tag{2.7}$$

And of the Laplacian

$$\nabla^2 u = \frac{\partial^2 u_x}{\partial x^2} + \frac{\partial^2 u_x}{\partial y^2} + \frac{\partial^2 u_x}{\partial z^2} \tag{2.8}$$

Gives

$$(\lambda + \mu)\frac{\partial \theta}{\partial x} + \mu \nabla^2 (\partial u_x) = \rho \frac{\partial^2 u_x}{\partial t^2} \tag{2.9}$$

For the x component of the equation of motion

A similar equation can be obtained for the y and z displacement components. The three equations can be combined using the Laplacian of the displacement field operator.

$$u\nabla^2 = (\nabla^2 u_x + \nabla^2 u_y + \nabla^2 u_z) \tag{2.10}$$

Into a single equation

$$(\lambda + \mu)\nabla(\nabla \cdot u(x,t)) + \mu \nabla^2 u(x,t) = \rho \frac{\partial^2 u(x,t)}{\partial t^2} \tag{2.11}$$

This is the equation of motion for an isotropic elastic medium written entirely in terms of displacement, with the dependence on position and time explicit. Eqn. 2.11 can be written using vector identity.

$$\nabla^2 u = \nabla(\nabla \cdot u) - \nabla \times (\nabla \times u) \tag{2.12}$$

To get

$$(\lambda + 2\mu)\nabla(\nabla \cdot u(x,t)) + \mu \nabla \times (\nabla \times u(x,t)) = \rho \frac{\partial^2 u(x,t)}{\partial t^2} \tag{2.13}$$

We express the displacement field in terms of two other functions, Φ and Y, which are potentials

$$u(x,t) = \nabla \Phi(x,t) + \nabla \times \mathrm{Y}(x,t) \tag{2.14}$$

In this representation, the displacement is the sum of the gradient of a scalar potential,(x, t), and the curl of a vector potential, $\mathrm{Y}(x,t)$, which are both $\Phi(x,t)$ functions of space and time. Since the vector identity

$$\nabla \Phi = 0 \tag{2.15}$$

Split the displacement field into two parts. The part associated with the scalar potential has no-curl or rotation and gives rise to compressional waves. Conversely, the part associated with the vector potential has zero divergences, causes no volume change, and corresponds to shear waves. Because taking the curl discards any part of the vector potential that would give rise to a non-zero divergence, we require that

the vector potential satisfy $\Upsilon(x,t) = 0$. Substituting the potential into equation 2.13 and rearranging the terms using equation Eqn. 2.15 yields.

$$(\lambda + 2\mu)\nabla(\nabla^2\Phi) + \mu\nabla \times \nabla \times \nabla \times \Upsilon = \rho\frac{\partial^2\nabla\Phi + \nabla \times \Upsilon}{\partial t^2} \tag{2.16}$$

Using Eqn. 2.13, the second part of Eqn. 2.16 simplifies to

$$(\lambda + 2\mu)\nabla(\nabla^2\Phi) + \mu\nabla \times \nabla \times \nabla \times \Upsilon = \rho\frac{\partial^2\nabla\Phi + \nabla \times \Upsilon}{\partial t^2} \tag{2.17}$$

$$\nabla \times \nabla \times \nabla \times \Upsilon = -\nabla^2(\nabla \times \Upsilon) + \nabla(\nabla \cdot (\nabla \times \Upsilon)) = -\nabla^2(\nabla \times \Upsilon) \tag{2.18}$$

Because the divergence of the curl is zero. After this substitution, the terms in eqn. 2.16 can be regrouped to give

$$\nabla\left[(\lambda + 2\mu)\nabla^2\phi(x,t) - \rho\frac{\partial^2\phi(x,t)}{\partial t^2}\right] = -\nabla \times \left[\mu(\nabla^2\phi(x,t) - \rho\frac{\partial^2\phi(x,t)}{\partial t^2}\right] \tag{2.19}$$

because the elastic constants do not vary with position, and the order of has no effect.

A solution to the equation can be found when both terms in the brackets are zero.

$$\nabla\left[(\lambda + 2\mu)\nabla^2\phi(x,t) - \rho\frac{\partial^2\phi(x,t)}{\partial t^2}\right] = 0 \tag{2.20}$$

The scalar potential satisfies.

$$\nabla^2\phi(x,t) = \frac{1}{\alpha}\frac{\partial^2\phi(x,t)}{\partial t^2} \tag{2.21}$$

with velocity $\alpha = \left[\frac{\lambda+2\mu}{\rho}\right]^{\frac{1}{2}}$ this solution corresponds to P waves or compression waves.

Similarly, the vector potential satisfies.

$$\nabla^2\Upsilon(x,t) = \frac{1}{\beta}\frac{\partial^2\Upsilon(x,t)}{\partial t^2} \tag{2.22}$$

with velocity $\beta = \left(\frac{2\mu}{\rho}\right)^{\frac{1}{2}}$ this solution corresponds to P waves or compression waves.

Waves on a string satisfied the wave equation.

$$\frac{\partial^2 u(x,t)}{\partial x^2} = \frac{1}{v^2}\frac{\partial^2 u(x,t)}{\partial t^2} \tag{2.23}$$

Describes the propagation of a scalar quantity in one-dimensional space. The scalar potential satisfies a similar scalar wave equation, except that the spatial variable x is in three dimensions. The vector potential, a vector quantity, satisfies the analogous wave equation in three dimensions.

The wave equations 2.20 and 2.22 are strictly valid only for a homogeneous medium because they were derived under the assumption that all derivatives of the elastic constants are zero. The wave equations are valid in any coordinate system.

2.2 Plane waves

The scalar wave equation in three dimensions,

$$\frac{\partial^2 \phi(x,t)}{\partial x^2} = \frac{1}{v^2}\frac{\partial^2 \phi(x,t)}{\partial t^2} \tag{2.24}$$

describes how the scalar field $\phi(x,t)$ propagates in three dimensions. It is a homogeneous wave equation with no forcing function acting to act as a source of waves. If there were, it would be a homogeneous scalar wave equation in three dimensions with a source term f(x,t).

$$\nabla\phi(x,t) - \frac{1}{v^2}\frac{\partial^2 \phi(x,t)}{\partial t^2} = f(x,t) \tag{2.25}$$

would apply.

The harmonic wave solution of the scalar wave equation in one dimension is

$$u(x,t) = A\exp^{(i\omega t \pm kx)} \tag{2.26}$$

can be generalized to solve the three-dimensional scalar wave equation. This solution, known as the harmonic plane wave, is written down.

$$\phi(x,t) = A\exp^{(i\omega t \pm \mathbf{k}\cdot\mathbf{x})} = A\exp^{(i\omega t \pm k_x x \pm k_y y \pm k_z z)} \tag{2.27}$$

Where x is the position vector, and $\mathbf{k} = (k_x, k_y, k_z)$ is now the wave vector, also called the wavenumber vector. This solution describes a plane wave propagating in an arbitrary direction given by the wave vector. To show this, we write $k = [k]\widehat{k}$, where $\widehat{k}$ is a unit vector along the direction of k; thus Eqn. 2.27 becomes

$$\phi(x,t) = A\exp^{(i\omega t \pm |k|\widehat{k})} \tag{2.28}$$

A plane wave propagating in the $\widehat{k}$ direction with velocity

$$v = \frac{\omega}{|\mathbf{k}|} \tag{2.29}$$

The wave vector describes two important properties of a propagating wave. Its magnitude gives the wavenumber and the spatial frequency, and its direction gives the direction of propagation. The wavefront, which at any given time has constant phase $(\omega t - \mathbf{k} \cdot \mathbf{x})$ and constant values of $\phi(x, t)$, are planes perpendicular to the direction of propagation (Fig. 2.1).

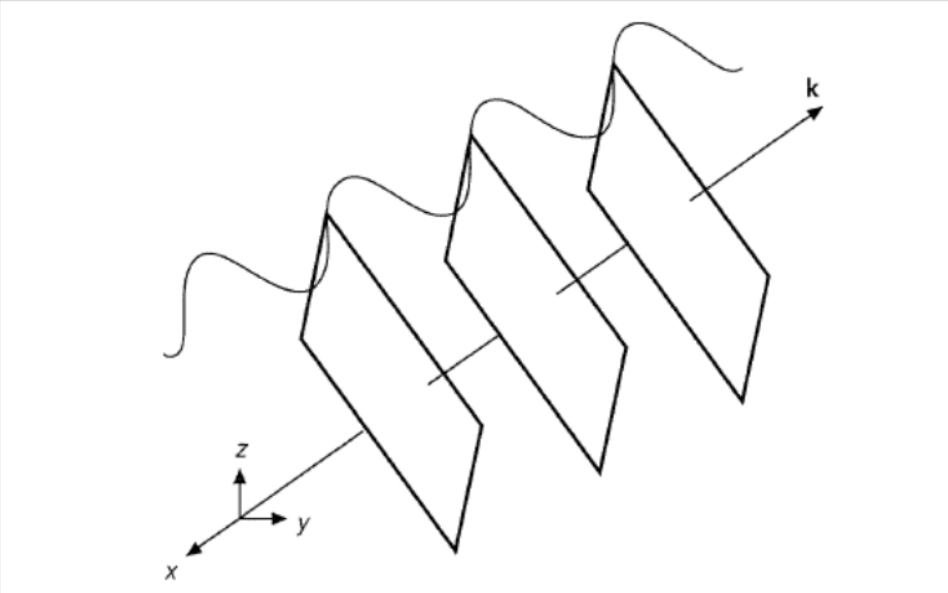

Figure 2.1: Wave fronts for the harmonic plane wave traveling in the direction indicated by the wave vector. The wavelength is $\lambda = 2\pi/|k|$ (Stein and Wysession, 2009).

Note that since all points on a plane perpendicular to the wave vector have the same value of $\mathbf{k} \cdot \mathbf{x}$, since this scalar product is the projection of $\mathbf{k}$ onto $\mathbf{x}$. The phase is periodic over a distance along the propagation direction equal to the wavelength, $2\pi/|k|$.

This solution of the three-dimensional scalar wave equation can be generalized to solve the vector wave equation in three dimensions,

$$\nabla^2 \Upsilon(x, t) = \frac{1}{v} \frac{\partial^2 \Upsilon(x, t)}{\partial t^2} \tag{2.30}$$

which describes the propagation of a vector field. In Cartesian coordinates, this breaks down into three scalar wave equations

$$\nabla^2 \mathrm{Y}_x(x,t) = \frac{1}{v}\frac{\partial^2 \mathrm{Y}_x(x,t)}{\partial t^2}$$

$$\nabla^2 \mathrm{Y}_y(x,t) = \frac{1}{v}\frac{\partial^2 \mathrm{Y}_y(x,t)}{\partial t^2} \tag{2.31}$$

$$\nabla^2 \mathrm{Y}_z(x,t) = \frac{1}{v}\frac{\partial^2 \mathrm{Y}_z(x,t)}{\partial t^2}$$

The harmonic plane wave solution to the vector wave equation is then.

$$u(x,t) = A\exp^{(i\omega t \pm k\cdot x)} \tag{2.32}$$

where, $\mathrm{Y}(x,t)$ and the constant **A** are vectors.

2.3 Spherical waves

A second solution of the three-dimensional scalar wave equation yields waves with spherical rather than planar wavefronts. To obtain this solution, we express a scalar potential, $\phi(x,t)$, and its Laplacian in spherical coordinates.

$$\nabla^2\phi(r,t) = \frac{1}{r^2}\frac{\partial}{\partial r}\left(r^2\frac{\partial\phi(r,t)}{\partial r}\right) + \frac{1}{r^2 sin\theta}\frac{\partial}{\partial\theta}\left(sin\theta\frac{\partial\phi(r,t)}{\partial\theta}\right) + \frac{1}{r^2 sin^2\theta}\frac{\partial}{\partial\theta}\left(\frac{\partial^2\phi(r,t)}{\partial\theta^2}\right) \tag{2.33}$$

We consider spherically symmetric solutions where ϕ is a function of time and the radius r, so only the $\frac{\partial\phi}{\partial r}$ term in the Laplacian survives. The spherically symmetric waves satisfy the homogeneous wave equation.

$$\nabla^2\phi(r,t) = \frac{1}{r^2}\frac{\partial}{\partial r}\left(r^2\frac{\partial\phi(r,t)}{\partial r}\right) = \frac{1}{v^2}\frac{\partial^2\phi(r,t)}{\partial t^2} \tag{2.34}$$

The space variable is the radius r rather than the position vector r. To solve this equation, we substitute

$$\phi(r,t) = \frac{\xi(r,t)}{r} \tag{2.35}$$

And get

$$\frac{1}{r}\left[\frac{\partial^2 \xi}{\partial r^2} - \frac{1}{v^2}\frac{\partial^2 \xi}{\partial t^2}\right] = 0 \tag{2.36}$$

Since the term in parentheses is the scalar wave equation in one dimension, any function of the form $\xi = f(r \pm vt)$ satisfies Eqn. 2.36 when $r \neq 0$. Thus any function of the form Eqn. 2.37 is a spherically symmetric solution of the scalar wave equation.

$$\phi(r,t) = \frac{f(r,t)}{r} \tag{2.37}$$

This solution describes spherical wave fronts centered at the origin $r = 0$, whose amplitude depends on the distance from the origin. The minus sign in the above equation represents waves diverging outward from a source at the origin, with the amplitude decaying as 1/r.

However, eqn.2.37 is not a solution of the homogeneous equation everywhere in space because it is infinite at r = 0. Physically this is because a wave propagating from a point must have been generated by a seismic source there. Thus the outgoing wave $\phi(r,t) = \frac{f(t-\frac{r}{v})}{r}$, is a solution of the inhomogeneous wave equation.

$$\nabla^2\phi(r,t) - \frac{1}{v^2}\frac{\partial^2\phi(r,t)}{\partial t^2} = -4\pi\delta(r)f(t) \tag{2.38}$$

This represents a point source at the origin with a time function f(t). The delta function $\delta(r)$ is zero except at $r = 0$, but its integral over a volume including the origin is 1. Thus integration over a volume, including the origin, shows that eqn. 2.37 is a solution to the inhomogeneous scalar wave eqn. 2.38 even at the origin.

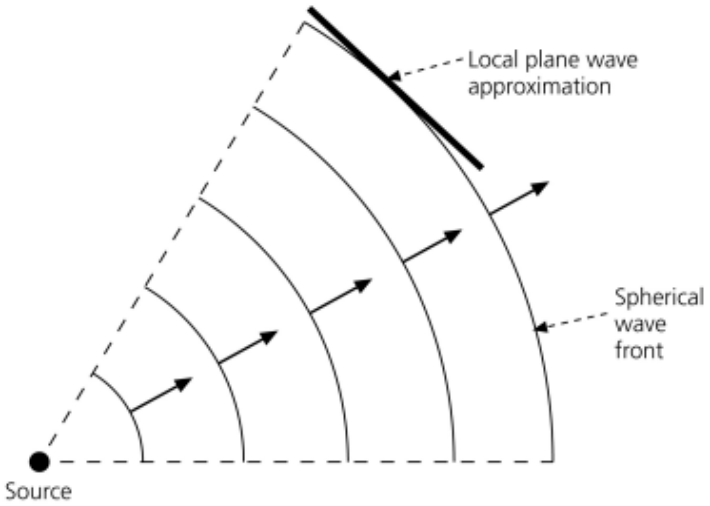

Figure 2.2: Spherical wavefront spreading out from a source (Stein and Wysession, 2009)

The spherical wave solution (eqn. 2.37) represents a continuous wave generated at the origin and explains the distance-dependent amplitude factor 1/r, which has no equivalent in the plane wave solution. As a spherical wave front, $4\pi r^2$ increases. The energy per unit area of the wavefront carried by a propagating wave is proportional to the square of the amplitude, and the energy per unit wavefront decays as $\frac{1}{r^2}$. This decay, called geometrical spreading, conserves energy (Fig. 2.2).

A plane wavefront can be regarded as a limit of a spherical wave far from the source because the spherical wavefront becomes almost planar. This approximation is often used in seismology when seismometers are far from earthquakes.

2.4 Body waves

Elastic waves propagate in the ground at the surface with velocity, frequency and amplitude depending on the elastic properties of the medium and the source. Seismic waves carry energy that is converted into stresses and deformations of the ground and, resulting in displacements (seismic shaking). Based on the type of stress and the deformation caused on in the ground to which they are subjected and how they propagate, seismic waves are classified as body waves (P and S waves) and surface waves (Love and Rayleigh waves).

We found earlier that the displacement can be decomposed into a scalar potential corresponding to P waves satisfying the scalar wave equation.

$$\nabla^2\phi(r,t) = \frac{1}{\alpha^2}\frac{\partial^2\phi(r,t)}{\partial t^2} \tag{2.39}$$

And a vector potential corresponds to S waves that satisfy the vector wave equation. To the same equation. 2.24, we apply the curl operator. The curl of the gradient of the scalar function θ is zero, and the curl of the displacement u(x,t) is the rotation vector ω. The curl of ω is equal to the gradient of the divergence, which is zero minus the Laplacian. The results are

$$\nabla^2\Upsilon(r,t) = \frac{1}{\beta^2}\frac{\partial^2\Upsilon(r,t)}{\partial t^2} \tag{2.40}$$

The equations 2.24 and 2.25 are wave equations for the scalar function θ and the vector function ω. The solutions of both equations represent waves propagating in the elastic medium, and the parameters α and β are their velocities. These velocities are functions of the elastic coefficients λ and μ and the density ρ.

Sinceθ represents changes in volume without changes in shape, solutions of the equation 2.24 correspond to compressional and dilational motion, or longitudinal waves,

also called **P waves**. Solutions of the equation 2.25 represent shear waves propagating with at velocity β. The medium changes shape but not volume since the divergence of ω is zero. These waves are called **S-waves**. Let us consider a plane wave propagating in the z-direction. The scalar potential for a harmonic plane P wave satisfying Eqn. 2.24 is

$$\Phi(z,t) = A\exp^{i(\omega t - kz)} \tag{2.41}$$

So the resulting displacement is the gradient.

$$u(z,t) = \nabla\phi(z,t) = (0,0,-kz)A\exp^{i(\omega t - kz)} \tag{2.42}$$

Which has a non-zero component only along the propagation direction z the corresponding dilatation is non-zero,

$$\nabla \cdot u(z,t) = -k^2 A\exp^{i(\omega t - kz)} \tag{2.43}$$

Therefore, there is a change in volume. Furthermore, as the wave propagates, the displacements in the direction of propagation cause the material to alternately compress and expand. Thus, the P-wave generated by the scalar potential is called a compression wave.

On the other hand, the S-wave, or shear wave, described by the vector potential

$$\nabla \cdot u(z,t) = (A_x + A_y + A_z)A\exp^{i(\omega t - kz)} \tag{2.44}$$

The curl gives the resulting displacement field.

$$u(z,t) = \nabla \times \Upsilon(z,t) = (-ikA_x + ikA_y + 0)A\exp^{i(\omega t - kz)} \tag{2.45}$$

whose component along the propagation direction z is zero. Thus the displacement associated with a propagating shear wave is perpendicular to the direction of propagation. Therefore, a shear wave causes no change in volume due to dilation. $\nabla \cdot u(z,t)$ is zero.

P-waves produce displacement in the direction of wave propagation and volume change. S-waves produce displacement perpendicular to the direction of wave propagation and deform the material without volume change. A compression wave is an example of a longitudinal wave because the propagating displacement varies in the direction of propagation. An example of a longitudinal wave is a sound wave in air, which is described as a compressional (elastic) wave in an ideal fluid. On the other hand, a shear wave is an example of a transverse wave because the propagating displacement field varies at a right angles to the direction of propagation. Electromagnetic waves are another well-known example of transverse waves.

The component of $Y(z,t)$ in the direction of wave propagation A_z has no effect on the displacement field because it is discarded with the curl . Only A_x and A_y contribute to the displacement. Since each displacement component depends on only one of these terms, there can be two independent shear wave fields. If A_x or A_y is zero, then there is only one y and one x-component of the displacement. Thus, shear waves can have two independent polarization, like other transverse waves, such as light.

In real applications, we define the z-axis as the vertical direction and orient the x-z plane along the great circle connecting a seismic source and a receiver. Plane waves propagating in the direct path between the source and receiver thus propagate in the x-z plane. The polarized directions of shear waves are defined as SV for shear waves with displacements in the vertical x-z plane and SH for horizontally polarized shear waves with displacements in the y-direction parallel to the Earth's surface as seen in the figure 2.3. Both have displacements perpendicular to the propagation direction and the other.

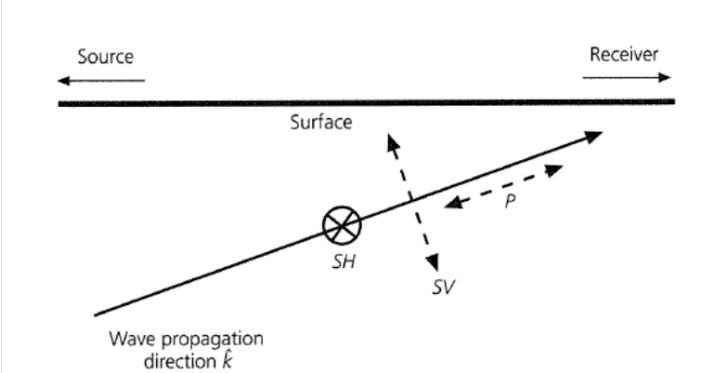

Figure 2.3: Displacement fields for plane P and S waves propagating in the x-z, a plane containing the source and receiver, where the z-axis is vertical.

P and SV waves are coupled when they interact with horizontal boundaries, while SH remains separate.

Seismometers record the horizontal motions in the north-south and east-west directions, which rarely correspond exactly to the SH and SV polarizations. As a result, data from the horizontal components of seismometers are often rotated. The direction connecting the source and the receiver, corresponding to the SV displacements, is called the radial direction, so a seismogram rotated in this direction is called the radial component. Similarly, the direction orthogonal to the component corresponding to the SH displacements, is called the transverse direction, so a seismogram rotated to in this direction is called the transverse component.

The definition of P wave velocity, termed as α and v_p

$$\alpha = \left[\frac{\lambda + 2\mu}{\rho}\right]^{\frac{1}{2}} = \left[\frac{K + 4\mu/3}{\rho}\right]^{\frac{1}{2}} \tag{2.46}$$

And S- wave velocity, terms β or v_s

$$\beta = \sqrt{\frac{\mu}{\rho}} \tag{2.47}$$

Shows that the seismic velocities depend in different ways on the elastic constants of the material. Since the stiffness μ and the bulk modulus K are positive, P waves travel faster than S waves. Thus, the first arriving wave of an earthquake is always compressional. As a result, the nomenclature P originally referred to the first arriving "primary" wave, while S referred to the "secondary" wave.

Although both velocities depend on the stiffness, the shear velocity does not depend on the bulk modulus K because these waves do not involve volume changes. Since the shear velocity is proportional to the square root of the stiffness, shear waves cannot propagate through the ideal (μ = 0) fluid. However, compressional waves propagate in the ideal fluid with a velocity proportional to $K^{\frac{1}{2}}$. Thus, only compressional waves can propagate through the Earth's outer core or the ocean.

Body waves propagate inside the earth with spherical or hemispherical wavefronts (depending on the position of the source) with increasing wider radius.

- **P-waves**: The particle motion of compressional waves is parallel to the direction of the wave propagation, causing dilation and compression. They are also called longitudinal waves (or compressional) waves because of the oscillations of the infinite planes into which the rock can be imagined to divide the rock body occur in the same direction of wave propagation (Fig. 2.4);

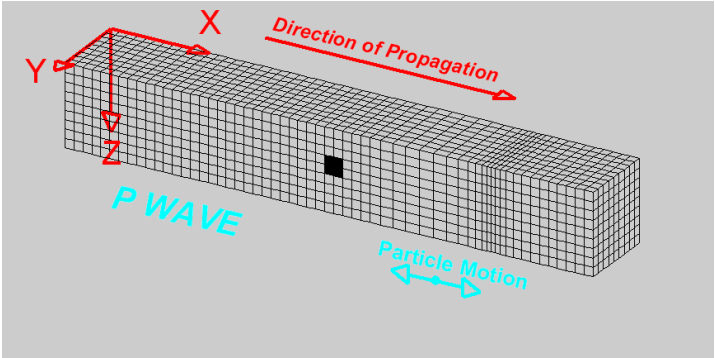

Figure 2.4: Compressional waves (Lore.trango, 2010)

- **S-waves**: The particle motion associated with shear waves is perpendicular to the direction of wave propagation and therefore therefore has both a vertical (SV) and a horizontal (SH) component. The transverse particle motion causes shear deformations (distortions) of volume elements within the medium (Aki, 1980) (as shown in Fig. 2.5).

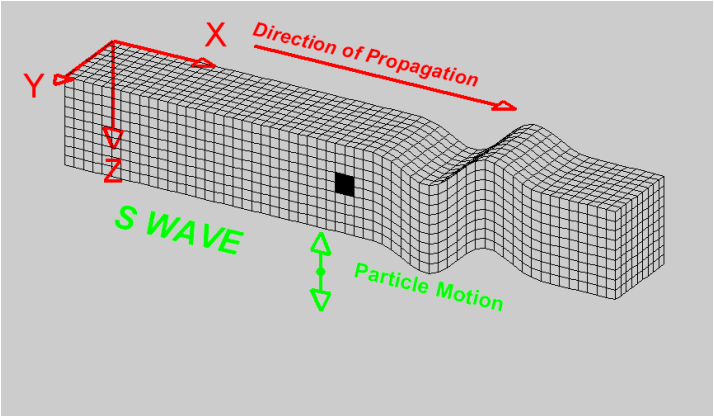

Figure 2.5: Compressional waves (Lore.trango, 2010)

The same result can be obtained from equations 2.2, and 2.3 for the potentials ϕ and ψ defined in equation 2.4. If we neglect the contribution of the body forces ϕ and ψ in equations 2.7 and 2.8 we obtain:

$$\nabla^2\phi = \frac{1}{\alpha^2}\frac{\partial^2\phi}{\partial t^2} \tag{2.48}$$

$$\nabla^2\psi = \frac{1}{\beta^2}\frac{\partial^2\psi}{\partial t^2} \tag{2.49}$$

In the absence of body forces, the potentials ϕ and ψ are also solutions of the wave equation. Since α and β are the velocities of the P and S waves, ϕ is the potential of the P waves and ψ is that of the S waves. The total elastic displacement u is the sum of the displacements of the P and S waves and can be written as:

$$u = u^P + u^S \tag{2.50}$$

Velocities α and β of P and S waves, respectively, as:

$$\alpha = \sqrt{\frac{(\lambda + 2\mu)}{\rho}} = \sqrt{\frac{M_V}{\rho}} \tag{2.51}$$

where M_V is the one-dimensional compressive stiffness modulus and ρ is the mass density.

$$\beta = \sqrt{\frac{\mu}{\rho}} \tag{2.52}$$

with μ stiffness shear modulus of the medium. The wave equation for P-waves can be rewritten as: K are p

$$\rho\frac{d^2\phi}{dt^2} = (\lambda + 2\mu)\nabla^2\phi \tag{2.53}$$

where ρ is the density, ϕ is the of P-wave potential, while λ is the *Lamè* constant. μ is the stiffness modulus, while λ is defined as $\lambda = K - 2/3\mu$, where K is the compressibility modulus.

The study of the dynamic equilibrium of the ideal elastic medium shows that the the volume of the seismic waves associated with states of compression or volumetric expansion, i.e., the P-waves, propagate in a direction parallel to the displacement of the volume element hit by the wave and with α velocity.

Instead, a direction perpendicular to the displacement instead characterizes S-waves. S-waves are characterized by a wave equation equal to:

$$\rho \frac{d^2\psi}{dt^2} = (\mu)\nabla^2\psi \tag{2.54}$$

Introducing $u^P = \nabla\phi$ and $u^S = \nabla \times \Psi$ we can write wave equations in terms of displacement u:

$$\frac{\partial^2 u_1}{\partial x_1^2} = \frac{1}{\alpha^2}\frac{\partial^2 u_1}{\partial t^2} \tag{2.55}$$

$$\frac{\partial^2 u_2}{\partial x_1^2} = \frac{1}{\alpha^2}\frac{\partial^2 u_2}{\partial t^2} \tag{2.56}$$

with u_1 and u_2 solutions of the wave equations. The ratio of α and β can only be expressed as a function of the Poisson ratio ν:

$$\frac{\alpha}{\beta} = \frac{\lambda + 2\mu}{\mu} = \frac{2(1-\nu)}{(1-2\nu)} > 1 \tag{2.57}$$

which shows that V_S is always smaller than V_P s. For ν = 1/4 (a typical value for several materials), $V_P = \sqrt{3} \cdot V_S$

A typical solution of the wave equations (2-9) and (2-10) is a harmonic function as:

$$f(x,t) = Ae^{(kx-\omega t)} + Be^{i(kx-\omega t)} \tag{2.58}$$

ω is the angular frequency, and k is the wave number. The speed of the wave propagation is $c = \omega/k$. Another form of the solution can be represented by using sine and cosine functions:

$$f(x,t) = Acos(kx - \omega t) + Bsin(kx - \omega t) \tag{2.59}$$

Chapter 3

Seismic data

3.1 Earthquake data sets

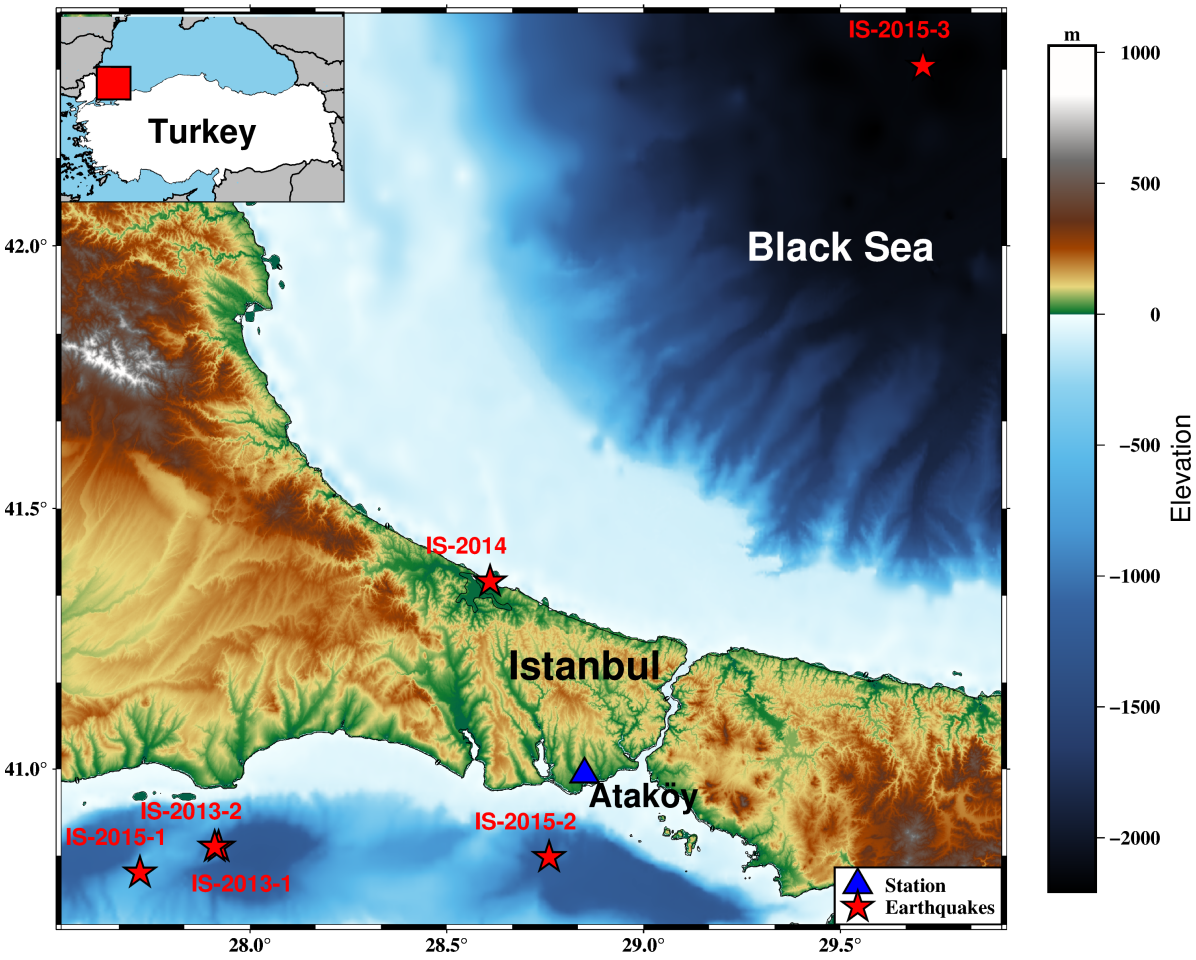

Figure 3.1: Epicenters of the earthquakes used in this study

In this study, we used a seismic data set (Table 3.1) consisting of seismic recordings from six earthquakes with magnitudes between Mw 3.7 and 4.8 (with epicentral distances between 20 and 165 km) that occurred between November 2013 and December 2015, four of which were located in the Marmara Sea region, as shown on the map (Fig.3.1). It is important to note mention that three of the six events (Table 3.1, events 4 – 6) occurred after the new dense SOSEWIN installation, and therefore only three of the six earthquakes are used to estimate the attenuation in the building.

The data from the SOSEWIN sensors, which have an initial sampling rate of 100 samples per second, are resampled using a MATLAB routine which is based on linear interpolation to have the same sampling rate as the borehole sensors, which have a sampling rate of 200 samples per second.

Table 3.1: List of events used in this study for the test site in Istanbul, Turkey

Event ID	Date	Time (UTC)	Location	Depth (km)	Magnitude (Mw)	Epicenter (Km)
IS-2013-1	27.11.2013	04:13:37	40.85 N, 27.92 E	9	4.8	80
IS-2013-2	27.11.2013	04:21:35	40.85 N, 27.91 E	7	4.0	80
IS-2014	05.02.2014	01:56:44	41.36 N, 28.61 E	12	3.7	45
IS-2015-1	28.10.2015	16:20:03	40.80 N, 27.72 E	16	4.6	100
IS-2015-2	16.11.2015	15:45:43	40.83 N, 28.76 E	8	4.3	20
IS-2015-3	15.12.2015	01:13:39	42.34 N, 29.71 E	30	4.1	165

3.2 Description of the study site

The seismic data for this study were acquired from a vertical downhole array of accelerometers installed in four wells boreholes in the Ataköy district of Istanbul, Turkey. Three are shallow boreholes with depths of 25, 50, and 70 m, depths and one deep borehole with a depth of 140 m (Figure 3.2a). In addition, one sensor was installed at the surface (0 m) (Parolai, 2012). The array was installed in December 2005 as part of a joint research project between the Kandilli Observatory and the Earthquake Research Institute (KOERI) of Bogazici University, Istanbul, Turkey, and the German Research Centre for Geosciences (GFZ).

Due to the malfunction, there are no seismic data records for some earthquakes from the sensor placed located 70 m downhole. Figure 3.2a shows the S-wave velocity structure at the test site. The shear wave velocity profiles were obtained by Parolai (2012) inverting the spectra of the deconvolved wavefields using earthquake data at

the site. In this part of the city, alluvial deposits (unconsolidated sediments composed of gravel, sand, silt, and clay) overlie of the Bakirköy Güngören Formation overlie the Paleozoic bedrock (Sørensen et al., 2006).

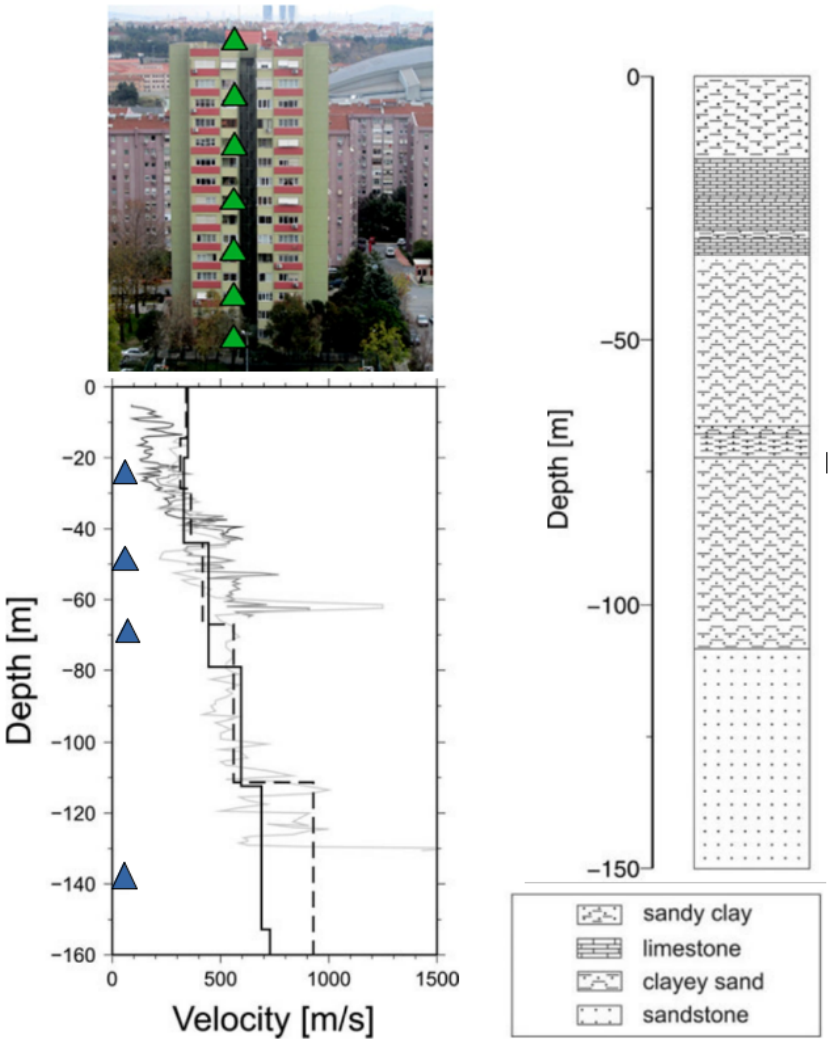

(a) Borehole and B22 building **(b)** Stratigraphy of the ground at Ataköy test site

Figure 3.2: Installations in the building B22 (green squares) and in the borehole (blue triangles) of the Ataköy, test site, Istanbul, showing a photograph of the building, the shear wave velocity profile obtained from the inversion of the spectra of the deconvolved wave field (Figures modified from Parolai et al. (2009), and Petrovic et al. (2018).

Another set of recorded seismic data from a vertical array of accelerometers was used from a 16-story (including one basement level) tunnel formwork (box-shaped steel in a prefabricated form that allows walls and slabs to be cast in a single construction operation) building.) The building, locally known as , "B22", is equipped with a SOSEWIN (Self-Organizing Seismic Early Warning Information Network) network

consisting of 15 stations (four of them connected to 5TC Güralp strong motion accelerometers) installed near the center of the building, and the fire escape staircase (Fig. 3.2a) on different floors since September 2015. The first SOSEWIN installation, consisting of only three SOSEWIN stations, was placed in the basement, the 8^{th} floor, and the roof was realized in the summer of 2013, and another station was added later.

The building is located about 50 m from the borehole, with a total height of about 45 m and an approximately square footprint with dimensions of 23.1 m and 9 23.9 m (see Fig. 3.2a). The building's exterior walls with windows were constructed of precast panels. The interior and the remaining exterior walls of the building are made of 15 and 20-cm thick reinforced concrete, respectively.

Figure 3.2b summarizes the geology of the shallow soil beneath the study site at Atakoy. In the first 15 m depth, the subsoil consists of light brown, hard gravelly sandy clay. The second layer from the surface contains limestone. Clay inter-layers were found at 35 m depth down, . From about 110 m down to the bottom of the deepest borehole (140 m), very dense layers of sandy clay/clayey sand layers were encountered.

Chapter 4

Methodology

4.1 S-coda envelope

As primary waves from earthquakes propagate through, their amplitude slowly decays leaving a tail after they have passed Aki (1969) coined the term "coda waves" for these observed continuous wave trains after the arrival of the primary wave , and it has since been used since then to describe the tail portion of regional seismograms. The word "coda" refers to all wave trains after each primary wave. Thus, the P-codas are means the waves between the direct P-waves and the S-waves, and the S-codas waves are the seismic waves following the direct S-waves. The S-coda waves start after the S-waves and are composed of incoherent waves scattered by inhomogeneities. Scattering requires that the scattered wave to travel a greater distance than the direct wave, so the scattered wave will arrives were after the direct wave. Consequently, the part of the seismic trace immediately after the arrival time will be dominated by the direct wave, and the scattered waves will dominate the coda of the seismic trace.

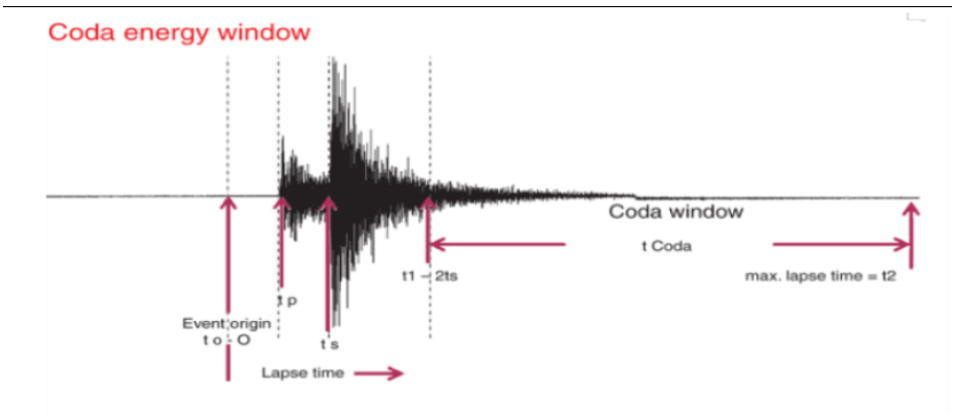

Figure 4.1: P and S-coda wave shown in a local seismogram (Kim et al., 2017)

Seismic coda results from the scattering of seismic waves by random heterogeneity in the Earth's crust (Aki, 1969). Coda waves are thought to be composed of scattered waves, as shown in Figure 4.1. Evidence for the generation of coda by scattering can be seen from the variation of the coda amplitude with the local geology at a recording site.

Therefore, the later part of the regional seismograms can be considered as the result of averaging over many samples of heterogeneities, suggesting a statistical treatment where in which a small number of parameters characterize the average properties of the heterogeneous medium.

The energy density of coda waves in a frequency band of width Δf with center frequency f is written as a three-component sum of the mean square particle velocity of the S-coda $\dot{u}_i^{S-Coda}(t, f_c)$ as

$$\begin{aligned} E^{S-Coda}(t, f_c) &= \left\langle \sum_{i=1}^{3} \frac{\rho_0}{2} |\dot{u}_i^{S-Coda}(t, f_c)|^2 + E \right\rangle_T \Delta f \\ &\approx \left\langle \sum_{i=1}^{3} \frac{\rho_0}{2} |\dot{u}_i^{S-Coda}(t, f_c)|^2 \right\rangle_T \Delta f \end{aligned} \tag{4.1}$$

where ρ_0 is the mass density, E is the elastic energy which is the potential energy stored in the medium, and $\langle \cdots \rangle_T$ is a moving time average over a few cycles around the central time t.

4.1.1 S-coda attenuation

The amplitude of coda waves is thought to decrease because of the seismic attenuation (both intrinsic and scattering) and because of the geometric propagation of the wave from. As reported by Rautian and Khalturin (1978), for a given region, the S-coda has a common amplitude decay curve for travel times greater than twice the S-wave travel time. The single-back scattering model was proposed by Aki and Chouet (1975) to explain the time dependence on the scattered energy density of the regional earthquakes in the short-period frequency band (1 - 20 Hz) as a function of the time from the of origin. For a source co-located with a receiver, the shape of the time-domain S-coda envelope filtered at a given frequency and the band centered at f can be explained by the exponential decay of the equation 4.2.

$$A(f, t) \propto \frac{1}{t^n} e^{-\frac{\pi f t}{Q_c(f)}} \tag{4.2}$$

where Q_c^{-1} is the coda decay factor, f is the center frequency, t is the propagation time and n is, 0.5 or 1 for surface and body waves, respectively.

The exponential decay term is characterized by the coda attenuation Q_c^{-1}, which is independent of the source and station location but dependent on the center frequency. The coda attenuation Q_c^{-1} characterizes the S-coda amplitude decay with lapse time. A larger Q_c^{-1} means more faster decay of the coda amplitude. It is possible to measure Q_c^{-1} by analyzing records obtained at a single station (Aki and Chouet, 1975).

4.1.2 Coda normalization

Coda normalization is based on the idea that at any given time the seismic energy is uniformly distributed in some a volume surrounding the source.

$$\left\langle |\dot{u}_{ij}^{Scoda}(t;f)|^2 \right\rangle_T \propto W_i^S(f)|N_j^S(f)|^2 \frac{e^{-Q_c^{-1}2\pi ft}}{t^n}, \tag{4.3}$$

where $\dot{u}_{ij}^{Scoda}(t;f)$ is the S coda velocity wave field at the i^{th} receiver filtered in a frequency band having the center frequency f, $W_i^S(f)$ is the energy radiation from the i^{th} source, $N_j^S(f)^2$ is the S wave site gain factor for the j^{th} site, and the power n = 2 for body waves.

4.2 Coda method

Seismic attenuation can be estimated from the decay of S-coda waves for local and regional events (Filippucci et al., 2021). Many observations, as summarized in Sato and Fehler (1998), show that the coda attenuation (Q_c^{-1}) is frequency dependent. Experimental Q_c^{-1} results are close to the direct Q_s^{-1}, which is interpreted as a kind of "regional constant", that measures the average attenuation characteristics of a given zone. Despite the Sato and Fehler (1998) demonstration that single-back scattering happens to have no valid physical assumption, Q_s^{-1} is close to a direct way of comparing the attenuation properties of different regions.

Frankel and Wennerberg (1987) using numerical solutions of the wave equation in heterogeneous media, showed that Q_c^{-1} estimated from the seismogram envelope under the assumption of single scattering is close to the true intrinsic attenuation. For $n = 0.5$, the equation 4.2 corresponds to a fully isotropic multiple scattering solution in 2D; in this case, Q_c^{-1} correctly takes the physical meaning of Q_i^{-1} of the medium Sato (1993).

4.3 Multi-Lapse Time Window Analysis

Several methods such as in Aki (1980), Frankel and Wennerberg (1987), Jacobsen (1987), and Taylor et al. (1986) have been proposed to determine the relative amounts of scattering loss intrinsic absorption.The most commonly used method is "the multiple lapse-time window analysis" (MLTWA) as proposed by Fehler et al. (1992). MLTWA is chosen due to its suitability to estimate scattering and intrinsic attenuation separately from the S-wave coda envelope's temporal and spatial distribution of the seismic energy.

The MLTWA method estimates scattering loss (Q_{sc}^{-1}) and intrinsic absorption (Q_i^{-1}) from S-wave envelopes (Hoshiba, 1991; Fehler et al., 1992). Several different scattering theories have been developed to model seismic coda. Previous models of coda wave generation models have often assumed spatial uniformity of seismic wave velocity. Wu and Aki (1985) was the first to consider multiple scattering into account to measure the relative contributions of scattering and intrinsic absorption to the total attenuation. His method is based on the radiative transfer theory, which is a theoretical model of energy propagation in a randomly heterogeneous elastic medium. The solution of the radiative transfer equation for scalar elastic waves describes the s-coda envelope as a function of the propagation time from the time origin.

The models proposed for describing seismic wave scattering are summarized as follows:

1. Weak scattering (single back-scattering) (Aki, 1969).
2. Multiple scattering model (e.g. Kopnichev (1977); Gao et al. (1983); Hoshiba (1991); Zeng et al. (1991); Sato (1993)).
3. Strong scattering or diffusion model (e.g., Wesley (1965)).

Weak and strong scattering models were based on the assumptions of isotropic scattering of scalar waves (no wave conversion), spherical source radiation, and a homogeneous, isotropic and random distribution of scatterers (Chouet, 1990).

For depth-dependent scattering attenuation and intrinsic absorption the s-coda envelope model Chouet (1990) synthesizes the coda envelope using the single-scattering approximation. Hoshiba (1991) estimates higher-order solutions numerically and Zeng et al. (1991) and Sato (1993) analytically. Hoshiba (1991) provided the numerical basis for the method by computing theoretical curves from a Monte Carlo simulation of multiple isotropic scattering.

Zeng et al. (1991) presented the analytical solution as

$$E(r,t) \approx E_0 e^{-\eta v t}\left(\delta\frac{\left(t-\frac{r}{v}\right)}{4\pi v r^2}+\eta_s\frac{H\left(t-\frac{r}{v}\right)}{4\pi v r t}ln\frac{1+\frac{r}{vt}}{1-\frac{r}{vt}}\right) + \left[cH\left(t-\frac{r}{v}\right)\left(\frac{3\eta_s}{4\pi v r t}\right)^{3/2} e^{\left[\frac{-3\eta_s r^2}{4\pi t}-\eta_i v t\right]}\right] \tag{4.4}$$

with

$$c = E_0\left[1-(1+\eta_s v t)e^{-\eta_s v t}\right]\left(\frac{4}{\sqrt{\pi}}\int_0^{\sqrt{3\eta_s v t}/2} e^{-\alpha^2}\alpha^2 d\alpha\right)^{-1}, \alpha = \frac{vt}{r}$$

where E_0 is the energy at t = 0, H is the Heaviside function, v is the wave velocity, $\eta = \eta_i + \eta_s$ and η_i and η_s are the intrinsic and the scattering attenuation, respectively. The scattering and scattering coefficients related to attenuation

$$\eta_s = \frac{2\pi f}{Q_{sc}.v} \tag{4.5}$$

and intrinsic attenuation coefficients

$$\eta_i = \frac{2\pi f}{Q_i.v} \tag{4.6}$$

where Q_s^{-1} is the scattering and $Q_i^{-1}$is the intrinsic attenuation, f is the frequency, and v is the S-wave velocity. Then the total is the combination of the scattering and the intrinsic attenuation:

$$Q_s^{-1} = Q_i^{-1} + Q_{sc}^{-1} \tag{4.7}$$

The attenuation due to intrinsic absorption and scattering is typically characterized by giving the values of the "seismic albedo", where B_0 is the ratio of scattering attenuation to the total attenuation, and the extinction length Le (i.e., the distance over which the primary S-wave energy is reduced by e^{-1}).

$$B_0 = \frac{\eta_s}{\eta_s + \eta_i} \tag{4.8}$$

$$Le^{-1} = \eta_s + \eta_i = (Q_i^{-1} + Q_{sc}^{-1})\frac{\omega}{v} \tag{4.9}$$

The seismic albedo ranges from 0 to 1; media with strong heterogeneity and no intrinsic absorption have an albedo close to one, and homogeneous media have zero seismic albedo.

Since no analytical solutions have been obtained (Bindi et al., 2006) for an inhomogeneous medium, such as a vertically layered medium Hoshiba (1997) numerically (using a Monte Carlo approach) synthesized the energy envelopes for a stratified earth model with assigned velocity, intrinsic, and scattering attenuation parameters for each layer (Figure 6.10). He synthesized the energy density E(r, t) of multiple scattered coda waves using many energy particles (each particle has unit energy at the source) whose random walks simulate the wave energy propagation and scattering process. Random walks of many particles simulate the seismic wave energy propagation and the scattering process. It is based on multiple scattering of energy particles under the hypothesis of isotropic scattering and uniform distribution of scatterers.

According to Fehler et al. (1992), MLTWA is based on two observations.

1. The early part of the seismogram is dominated by the direct S-wave, whose amplitude controls the total attenuation of the media.
2. S-coda consists entirely of scattered S-waves whose amplitudes of which are controlled by the total scattering coefficients.

The strategy of the MLTWA method is to minimize the simultaneous discrepancy between the observed seismic energy integrals and those predicted by theory. Therefore, the MLTWA technique measures the seismic wave energy as a function of distance and frequency for three consecutive time windows (Fig. 4.2). To do this, MLTWA first selects three seismogram windows, each 15 s wide, and a reference window of 5 s in the s-coda envelope. The figure 4.2 shows the three time windows and a reference window for the integrated energy calculations.

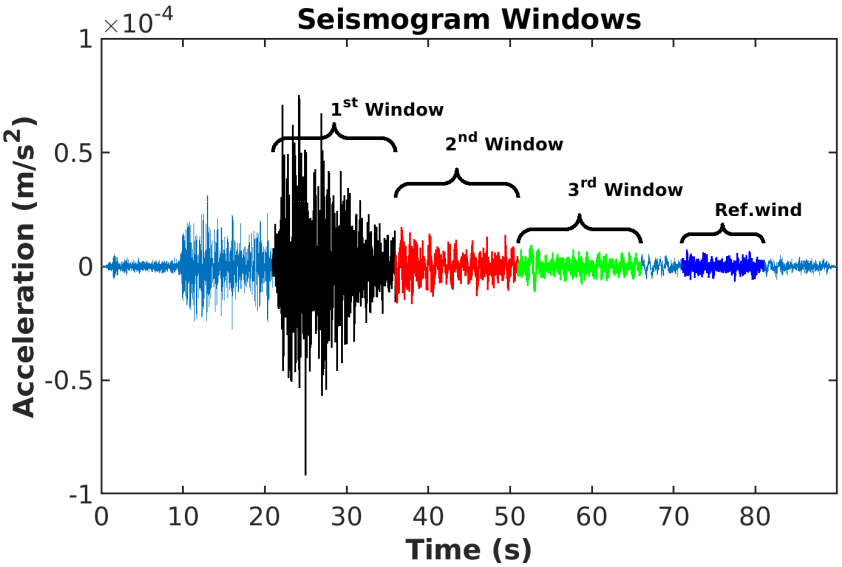

Figure 4.2: Seismograms of an event with three windows and a reference time window for MLTWA.

Eqn. 4.10 is used to calculate the time integral of the energy density for each time window, yielding the following three energy curves as a function of the hypocentral distance and frequency :

$$
\begin{aligned}
EI_1(f) &= \int_{ts}^{ts+15s} |\dot{u}^S(t,f)|^2 dt, \\
EI_2(f) &= \int_{ts+15}^{ts+30s} |\dot{u}^S(t,f)|^2 dt, \\
EI_3(f) &= \int_{ts+30}^{ts+45s} |\dot{u}^S(t,f)|^2 dt,
\end{aligned}
\tag{4.10}
$$

Each seismic integral is normalized by the average coda energy over in a fixed reference time interval of 5 seconds beginning at t_{1c} and ending at t_{2c}, where $t_{1c} \gg 2t_S$ (where,t_S is the S-wave travel time, and t_{1c} and t_{2c} are the start and end lapse times of the reference window in the s-coda, respectively) (Bianco et al., 2005) using the coda normalization method (Aki, 1980).

Coda normalization is based on the idea that the seismic energy is uniformly distributed at the the coda of S waves, it removes the effect of different sources and site amplification effects. Finally, $E_{(i)}(r,f)$ are corrected for geometrical spreading multiplying by the square of the hypocentral distance.

$$
E_{(i)}(r,f) = \frac{EI_{(i)}(f)}{EI^{Scoda}(f)} \cdot 4\pi r^2 \quad for \quad i = 1,2,3,... \tag{4.11}
$$

Chapter 5

Geophysical inversion

Geophysical data inversion involves the search for the optimal set(s) of Earth model parameters that can be used to compute synthetic data-matched observations. A defined misfit function is often used to measure the data misfit (or fitness). Optimization methods search for a minimum (optimal) value of a misfit function. Global optimization refers to finding the best set of parameters that are to the global minimum of a function of multiple parameters.

To test the validity of the inversion strategy, synthetic data are generated for a hypothesized model and compared with the observed data. If the agreement between observed and synthetic data is acceptable, the model is accepted as the solution; otherwise, the model is modified. The synthetics are recalculated and compared with the observations according to the inversion scheme. This iterative forward modeling process is repeated until an acceptable match between data and synthetics is obtained. Thus, the main task of inversion is to find a model that best explains the observed data.

The essential elements of a model-based nonlinear inversion algorithm are data, model, forward problem, objective function, and optimization method. We restrict ourselves the discrete data **d** and the model **m** defined by the following vectors

$$\begin{aligned} \mathbf{d} &= [d_1, d_2, d_3 \cdots d_N]^2 \\ \mathbf{m} &= [m_1, m_2, m_3, \cdots m_M]^2 \end{aligned} \tag{5.1}$$

In general $N \neq M$. The forward problem can be represented by the following equation

$$d^{syn} = g(m) \tag{5.2}$$

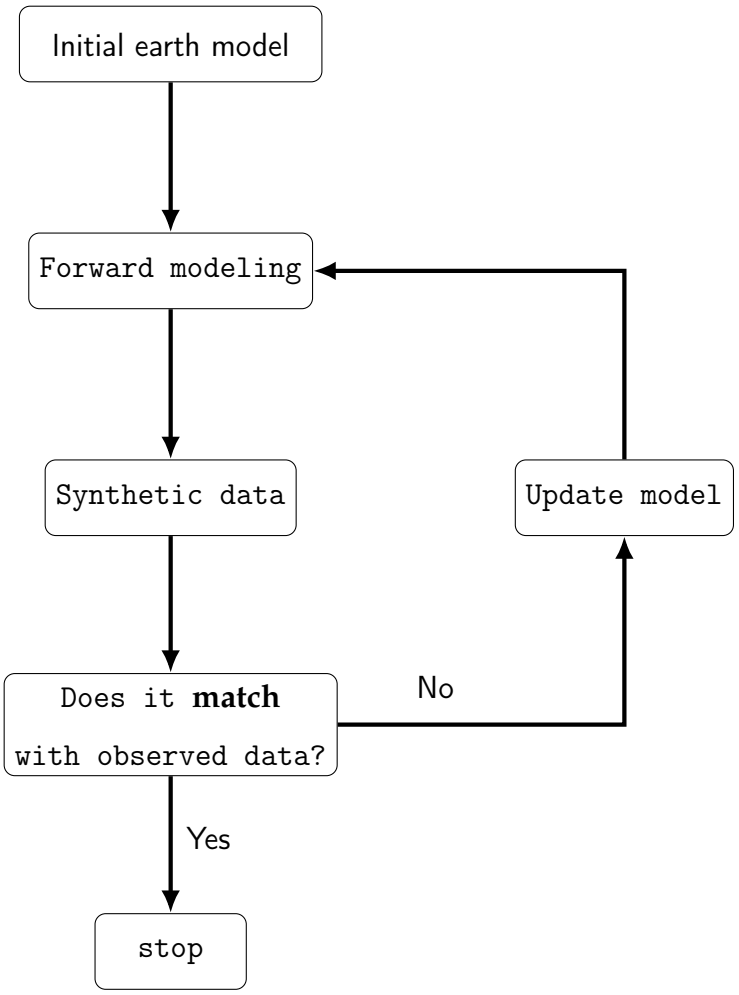

Figure 5.1: Principle of model-based inversion by optimization (modified from Sen and Stoffa (2013)).

where g is a nonlinear forward modeling operator that operates on the model vector to produce the synthetic data vector d^{syn}. The misfit function measures a misfit between the observed and synthetic data using an appropriately defined norm. The data residual is given by

$$\Delta \mathbf{d} = d^{obs} - d^{syn} \tag{5.3}$$

where d^{obs} is the observed data vector and the data misfit norm can be written as

$$\Delta \mathbf{d} = \sum_{i=1}^{N} \left[(\Delta d_i)^2 \right]^{\frac{1}{2}} \tag{5.4}$$

Which is the least squares minimization approach.

The goal of an optimization algorithm is to find search for the minimum of an objective function. The objective function may have multiple local minima; the minimum

of all the local minima is called the "global" minimum (e.g., Gill et al. (1981)). In most applications, once an objective function has been defined, the goal is to find the global minimum of the objective function. Figure 5.1 shows a flowchart of an optimization process.

Optimization methods are broadly divided into two categories: local optimization and global optimization. The global optimization methods are mostly based on stochastic rules and use more global information about the misfit surface to update its their to current position. There are different types of global optimization methods, such as Grid Search (GS), Simulated Annealing (SA), Genetic Algorithms (GA), Neighborhood Algorithms (NA), and Particle Swarm Optimization (PSO) (Kirkpatrick, 1983; Menke, 2012).

5.1 Grid search

One strategy for solving a nonlinear inverse problem is to examine exhaustively consider “every possible” solution and choose the one with the smallest error E(m). Of course, it is impossible to examine "every possible" solution; but it is possible to examine a large set of trial solutions. This procedure is called a grid search when the trial solutions are drawn from a regular grid in model space. An example of nonlinear inversion of a problem with a two-parameter problem is shown in the figure 5.2.

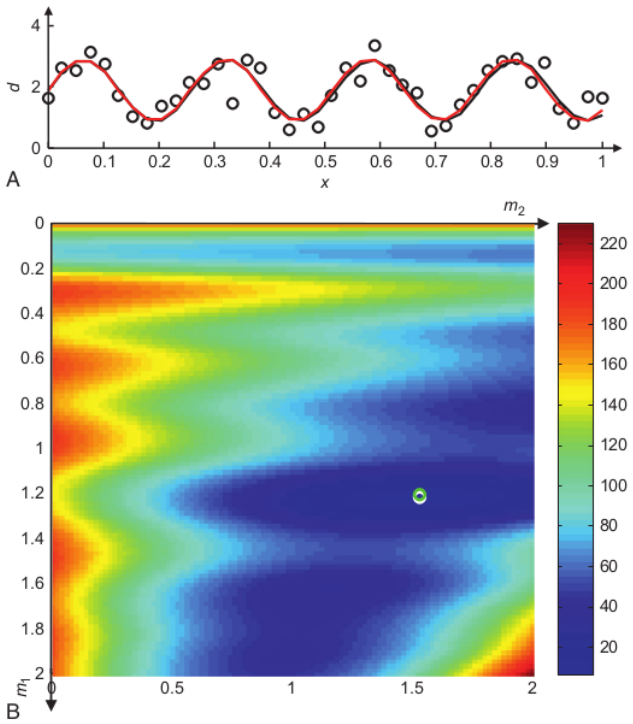

Figure 5.2: Example of grid search to solve a non-linear problem (taken from Menke (2012)).

Grid search is most practical when the number of model parameters is small, say M < 7. The grid is M-dimensional, so the number of trial solutions is proportional to L^M, where L is the number of trial solutions along each grid dimension. The forward problem d = g(m) can be computed fast enough that the time needed to compute L^M of them is in a reasonable range.

5.2 Simulated annealing

Simulated annealing is an optimization method first proposed by Kirkpatrick (1983). It is a statistical technique for finding optimal solutions to complex nonlinear optimization problems. The concept of simulated annealing is inspired by the physical annealing of metals. In the physical annealing of metals, an ordered minimum energy crystal structure develops as the metal slowly cools from its red-hot state. Atomic motion in hot metal is completely dominated by random thermal fluctuations, but as the temperature gradually decreases, interatomic forces become increasingly important. Eventually, the atoms become a crystal lattice representing a minimum energy configuration.

The simulated annealing algorithm starts with an initial model $\mathbf{m}_0$, with the corresponding error $E(\mathbf{m}_0)$. A test solution $\mathbf{m}^*$ with the corresponding error E($\mathbf{m}*$) , which

is in the neighborhood of **m**(p), by drawing an increment $\Delta\mathbf{m}$ to **m**(p) from a Gaussian distribution. The corresponding energy (objective function value) $E(\mathbf{m}_{new})$is then calculated and compared against the initial error ($E(\mathbf{m}_0)$). If the new error is smaller than the initial error, the new error is considered good. In this case, the new error is accepted and unconditionally replaces the initial error. However, if the energy of the new state is greater than the initial state then m_{new} is accepted with the probability of $e^{(\frac{-E(\mathbf{m}-E(\mathbf{m}_0)}{T})}$, where T is a control parameter called the annealing temperature that controls whether the "bad" model should be transferred to the new model.This completes an iteration.

The rule for accepting a probability, thatallows Simulated Annealing to get stuck in local minima. This process is repeated many times by gradually lowering the annealing temperature. Hopefully, a global minimum can be found with a carefully defined cooling schedule. For example, one can choose a linear or a logarithmically decreasing cooling scheme. The trade-off here is between the computational demand and the accuracy of the result. Fast cooling will not produce a crystal (the algorithm gets stuck in a local minimum), and slow cooling takes a long time but may eventually find the global minimum. The simulated annealing process is summarized as a flowchart in Figure **??**. Figure 5.3 shows an example of a nonlinear problem solved using simulated annealing inversion.

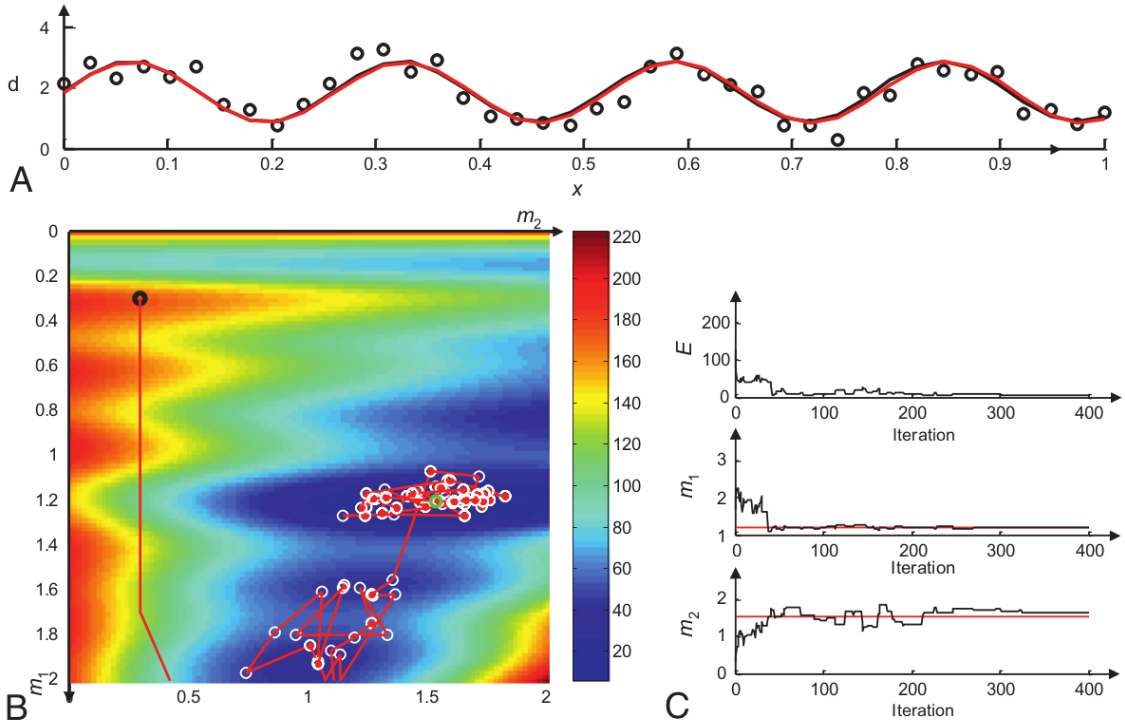

Figure 5.3: Example of simulated annealing algorithm used to solve non-linearly curve-fitting problem (taken from Menke (2012)).

Previous studies, such as in Bindi et al. (2006), have used grid search methods to min-

imize the residuals in MLTWA. However, this method has limitations in estimating the attenuation parameters within each layer for media with more than two layers due to the computational constraints imposed by the extensive computation involving the multilayer. To overcome this problem we have developed an inversion program that uses a simulated annealing algorithm (Kirkpatrick, 1983) and is applied to find the scattering and intrinsic attenuation coefficients that simulate theoretical energy integral that fits the observed energy integrals. The simulated annealing program is combined with the grid search procedure to estimate attenuation coefficients that simulate the theoretical energy density that best fits the observed seismic energy integrals. First, the grid search is used to estimate the range of parameters that give the global minimum. Once we had narrowed down the range of model parameters, we used this range for the simulated annealing inversion.

Figure 5.4 shows a flowchart of the simulated annealing algorithm used to write the inversion program in this study.

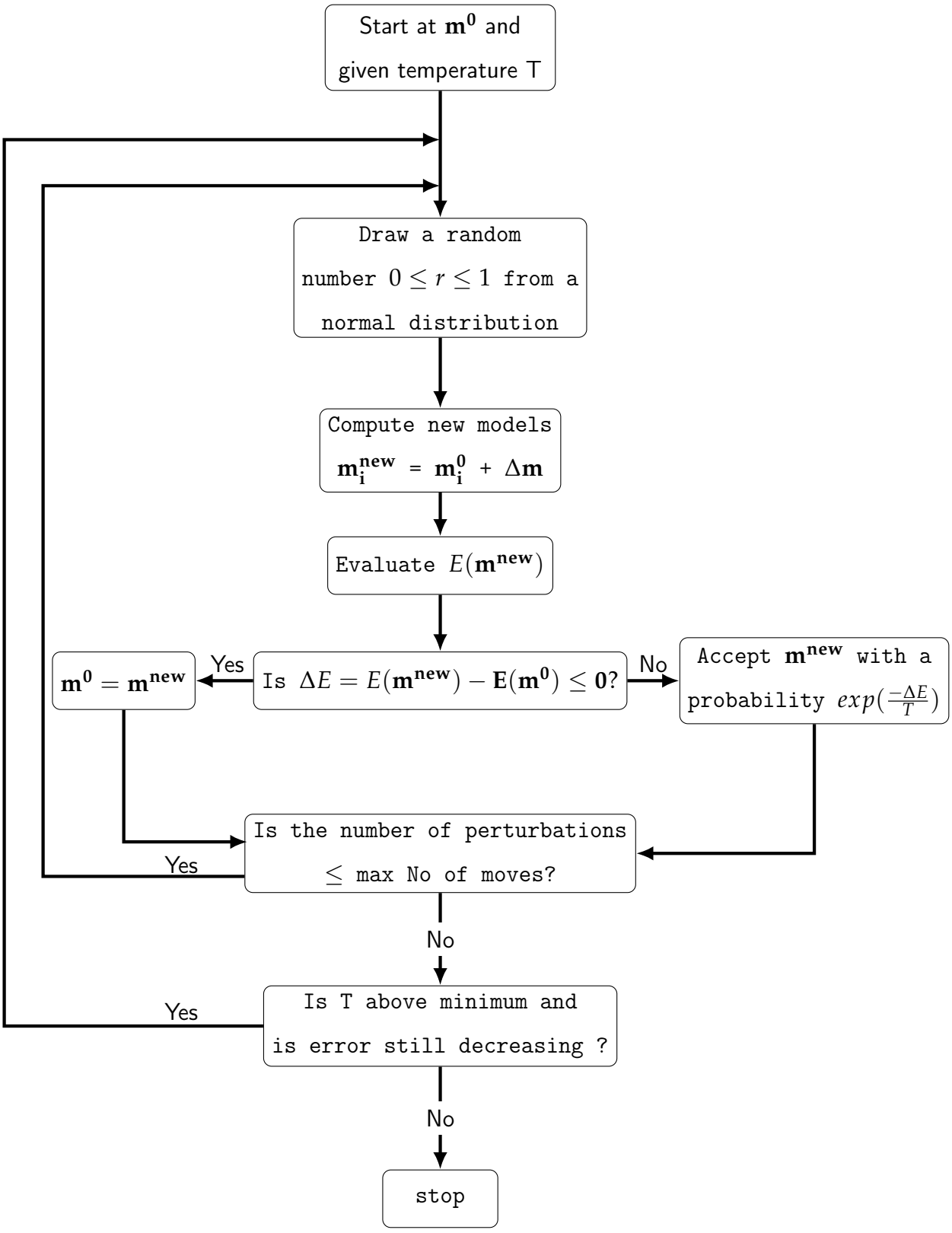

Figure 5.4: A flowchart for global optimization by simulated annealing (Figure modified from Odziemczyk (2020)).

Chapter 6

Data analysis and results

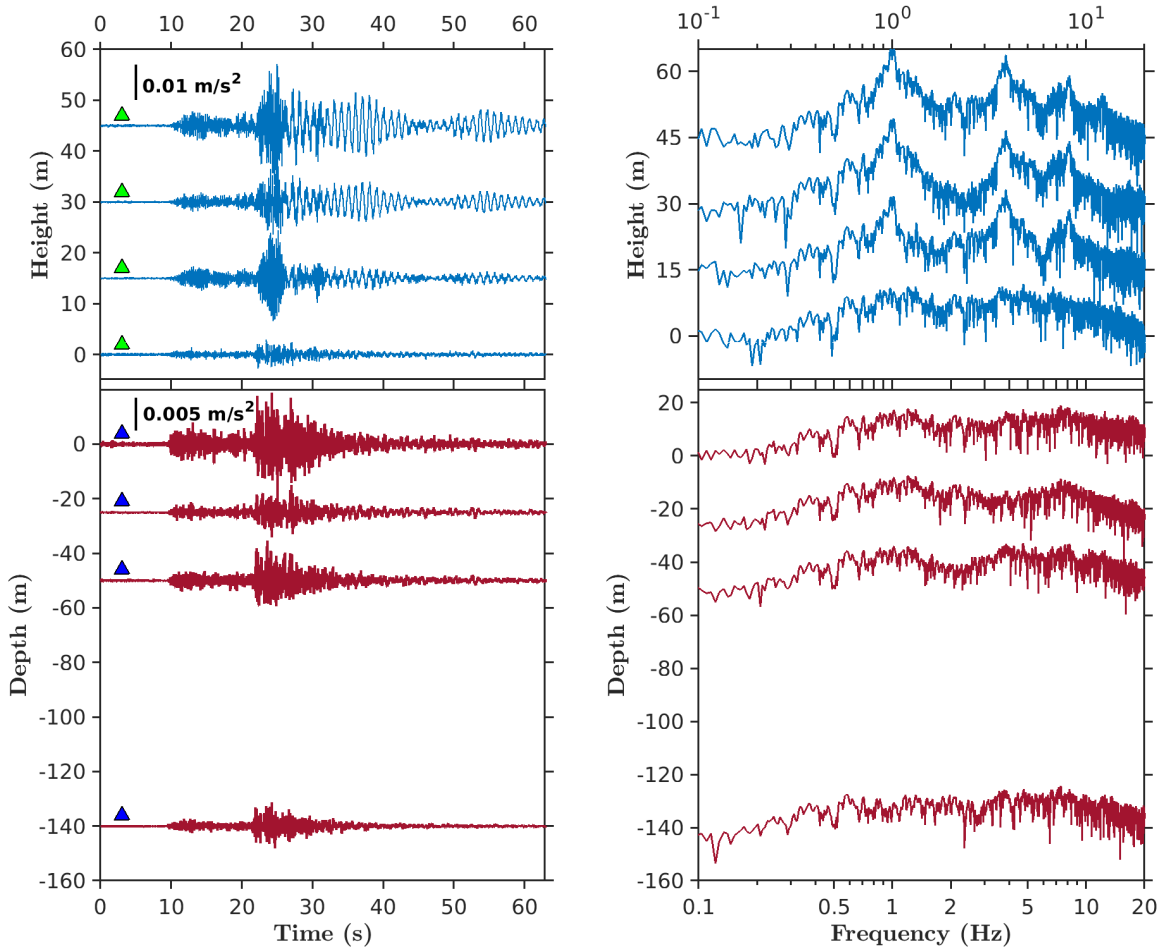

Figure 6.1: **(a)** An example of a vertical array of accelerograms(E-W component) from borehole sensors and buildings from 2015 Istanbul earthquake. **(b)** Spectra of accelerogram recorded from sensors

6.1 Attenuation from the coda method

$Q_c^{-1}(f)$ can be easily estimated from the recorded seismograms by fitting the envelopes of the bandpass filtered seismic traces to $A(f,t) \propto \frac{1}{t^n} e^{-\frac{\pi f t}{Q_c(f)}}$. We estimate $A(f,t) \propto \frac{1}{t^n} e^{-\frac{\pi f t}{Q_c(f)}}$ at the frequency f_c using the relationship

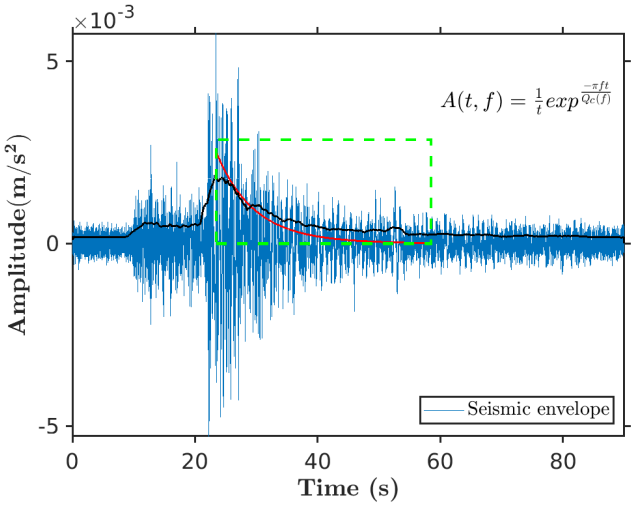

Figure 6.2: An example of a seismogram (in blue) analyzed for the estimation of Q_c^{-1}. The S-coda envelope is superimposed (dark lines) on the filtered trace. The part of the coda envelope in the green dashed square is used in this study to in estimate Q_c^{-1}.

$$A_{obs}(f,t) = \sqrt{H(S)^2 + S(t)^2} \tag{6.1}$$

where S(t) is the trace filtered at fc, H(S) is the Hilbert transform of t he trace itself, and t starts at $2t_s$ (where t_S is the S-wave travel time) and ends when the coda signal reaches the noise level.

We set the end coda at the time point of the seismogram when had a signal to noise ratio of 5. In this way, the average coda duration was 65 s from the start time.

Q_c^{-1} estimated by the Coda method for the study area. This is done by filtering the coda waves in the frequency bands centered at fc from 1 to 16 Hz, with a bandwidth ranging from $fc/2$ to $\sqrt{2}\ fc$. Then we do a least-squares fit of the envelope to eqn. 4.2 with n = 1.

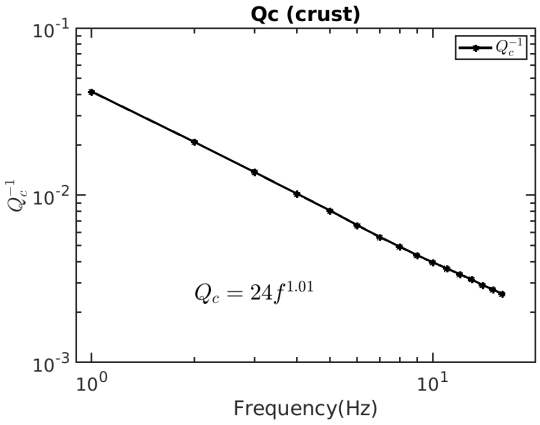

Figure 6.3: Attenuation s-coda of the crust beneath Marmara region using coda method.

Figure 6.2 shows an example of the filtered waveforms with the the relative envelope.

Table 6.1: Attenuation parameter results from the inversion

Frequency (Hz)	g	h	Qsc	Qi	Qs	Le^{-1}	B0
1	0.097	0.037	17.5	45.4	12.6	0.134	0.722
2	0.090	0.043	37.4	78.6	25.3	0.134	0.677
3	0.114	0.045	44.7	114	32.1	0.150	0.718
4	0.092	0.043	74.0	156	50.3	0.135	0.069
5	0.094	0.051	90.0	166	58.3	0.145	0.648
6	0.091	0.053	111.6	299	75.3	0.135	0.672
7	0.073	0.053	161.2	220	93.1	0.127	0.577
8	0.064	0.030	211.8	445	143.5	0.094	0.677
9	0.059	0.039	255.5	329	153.3	0.099	0.599
11	0.059	0.040	312.7	467	187.1	0.099	0.599
13	0.059	0.039	369	552	221.6	0.099	0.599
15	0.069	0.039	374.9	644	237.1	0.107	0.632

Qc increases as a function of frequency according to the power law $Qc = Q_0 f^n$ where Q_0 is the value of Qc at 1 Hz and n is the frequency dependence coefficient. The average attenuation law for the is $Qc = 24f^{1.01}$ (Fig. 6.3).

6.2 Attenuation from MLTWA

For this study, seismic energy integrals as a function of frequency and distance are calculated from four accelerograms from vertical arrays of sensors installed in boreholes and four accelerograms recorded by sensors installed on different floors of buildings about 50 m away from boreholes at the Ataköy test site. An example of an array of accelerograms from the 2015 Istanbul earthquakes is shown in figure 6.1a.

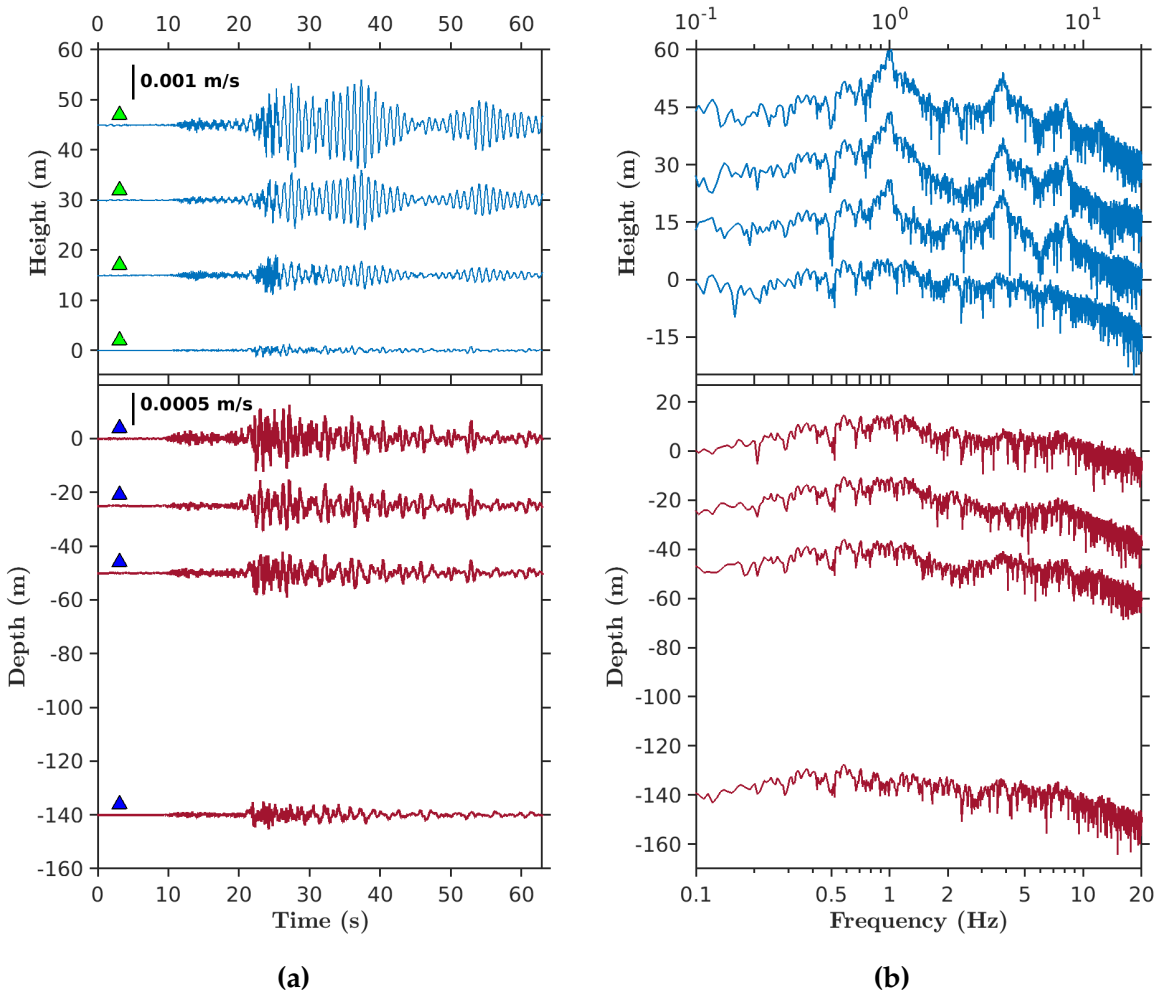

Figure 6.4: **(a)** Velocity seismograms and **(b)** their spectra converted from accelerograms

Recorded raw accelerograms must be converted to velocity seismograms for seismic energy calculation. The calculation of velocity seismograms begins with the preprocessed raw accelerograms. Preprocessing begins by removing trends or systematic distortions from the raw accelerogram as it is recorded. Filtering was performed to remove the unwanted noise from the seismograms and to extract the seismic energy of our preferred frequency range. Next, the accelerograms are filtered with 2^{nd} order Butterworth bandpass filters between the 0.1 Hz and 60 Hz frequency ranges. Finally,

the velocity seismograms are computed by time integration of the preprocessed accelerograms.

Figure 6.4 shows the converted the velocity seismograms from the accelerograms and Fourier spectra of the velocity seismograms.

Three consecutive seismogram windows and a reference window are selected for MLTWA analysis. The first window starts at ts (s-wave arrival time) and is 15s wide. The second seismic window is from 15 s to 30 s, and the third is from 30 s to 45 s. The reference window for normalization of the three seismic windows is selected in the coda of the seismogram between 57 s and 62 s from ts.The 15 s window length is chosen so that the first window contains a significant contribution of direct S-wave energy and the last two windows contain mainly the contribution of scattered energy.

For the four seismogram windows, 2% cosine tapering is applied at the beginning and end of the seismograms to reduce spectra leakage when the Fourier transform is performed on the seismogram windows. A Fast Fourier Transform (FFT) is performed on each seismogram window to compute the Fourier amplitude spectra. The amplitude spectra for each time window are smoothed by applying the Konno-Ohmachi window with ($b = 60$) using eqn. 6.2 (Konno and Ohmachi, 1998) (see fig. 6.6a). Then the seismic energy spectra are calculated from the squares of the smoothed amplitude spectra of each window as shown in the figure 6.6b.

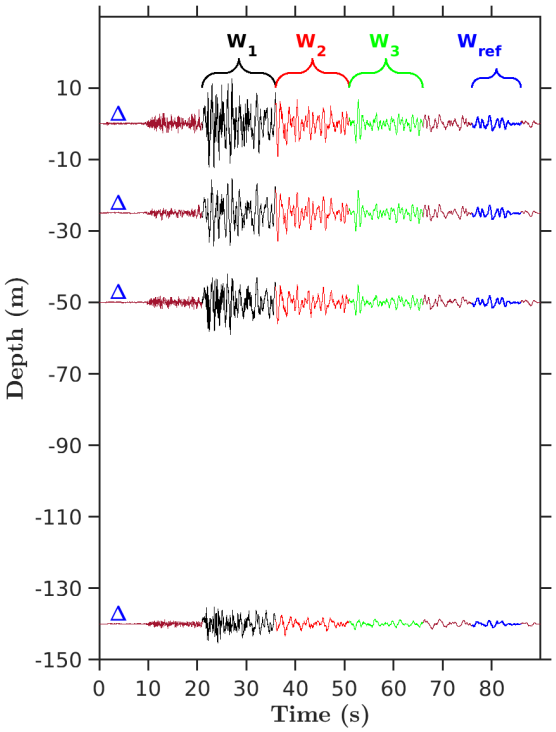

Figure 6.5: A vertical array of velocity seismograms with three 15 s seismogram windows and a 5 s reference window. The black part of the seismogram represents the first window, red the second window and green the third, and blue the reference window.

$$W_B(f, f_c) = \left[\frac{sin(log_{10}(\frac{f}{f_c})^b}{log_{10}(\frac{f}{f_c})^b}\right]^4 \tag{6.2}$$

where b is the bandwidth coefficient,
and f and f_c are frequency and
a center frequency, respectively.

The b-value controls the degree of smoothness of the the amplitude spectra, with

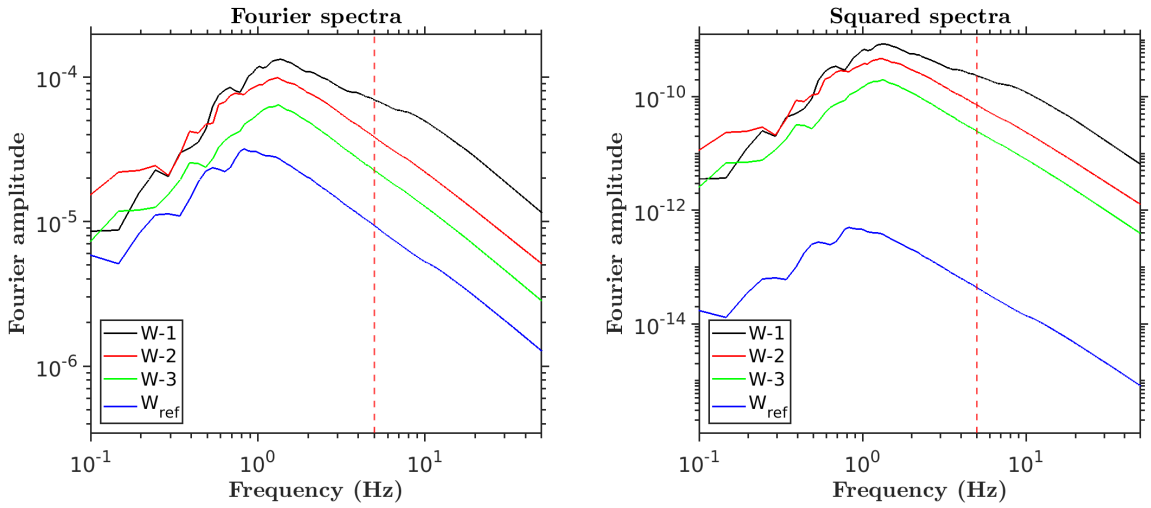

(a) **(b)**

Figure 6.6: An example of **(a)** Smoothed Fourier spectra of four windows from a single seismogram First (Black), second (red), third (green) and reference window (blue)). **(b)** corresponding squared spectra.

lower b-values resulting in under-smoothed spectra and higher values resulting in over-smoothed spectra. Choosing the of the appropriate b-value determines the value of the seismic energy integral and thus the stability of the inversion.

The seismic energy spectra of the first three windows are normalized to the seismic energy spectra of the reference window using the coda normalization method (Aki, 1980). Seismic energy spectra at the station are normalized to their reference coda energy. To account for the seismic energy loss due to the effect of geometrical spreading, the seismic energy integrals at each station are then multiplied by $4\pi r^2$. The seismic energy integral at the selected frequency can be obtained from the energy spectra ($E_1(f)$, $E_2(f)$, $E_3(f)$) at the preferred frequency.

Finally, the seismic energy integrals as a function of distance are computed for multiple sensors in the borehole and the building ($E_1(r,f)$, $E_2(r,f)$, $E_3(r,f)$) from a single earthquake. The whole process is repeated to obtain the seismic energy integrals for each station. In this case, the distances r are the depths of the sensors in the borehole from the surface and the height of the accelerograms in the building under study.

The seismic energy integral for an earthquake event is calculated from the average of the seismic energy calculated from the E-W and N-S components of the vertical array seismograms. The mean seismic energy integral (E(r, f)) is then calculated from an average of the energy integral of six earthquakes (values ranging from 3.7 to 4.8 Mw) that occurred around Istanbul, Turkey (see Fig. 3.1).The calculated mean seismic energy integral is shown in Fig.6.8.

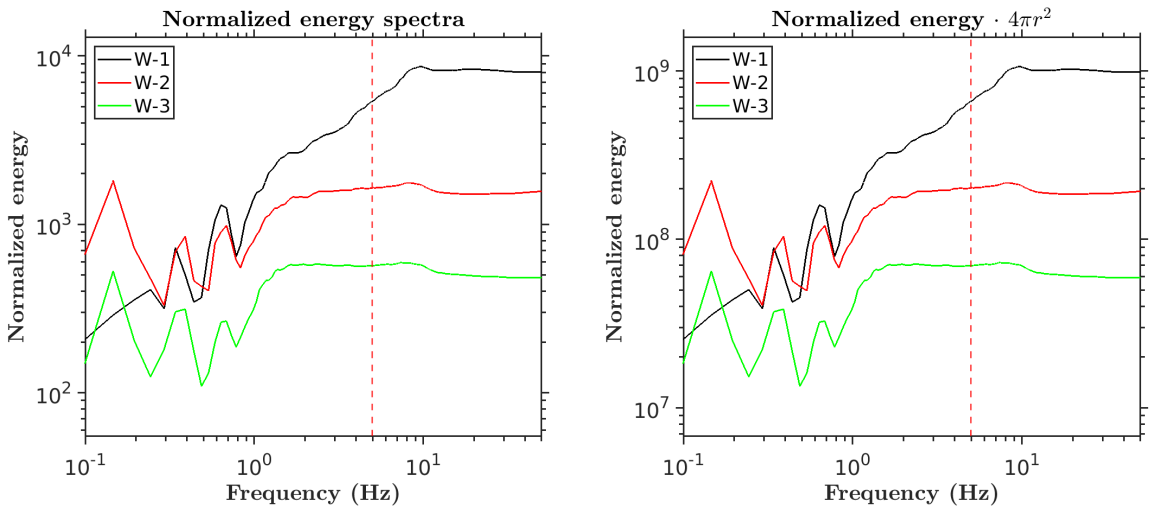

Figure 6.7: Normalized energy spectra and spectra of energy corrected for geometrical spreading of the three windows.

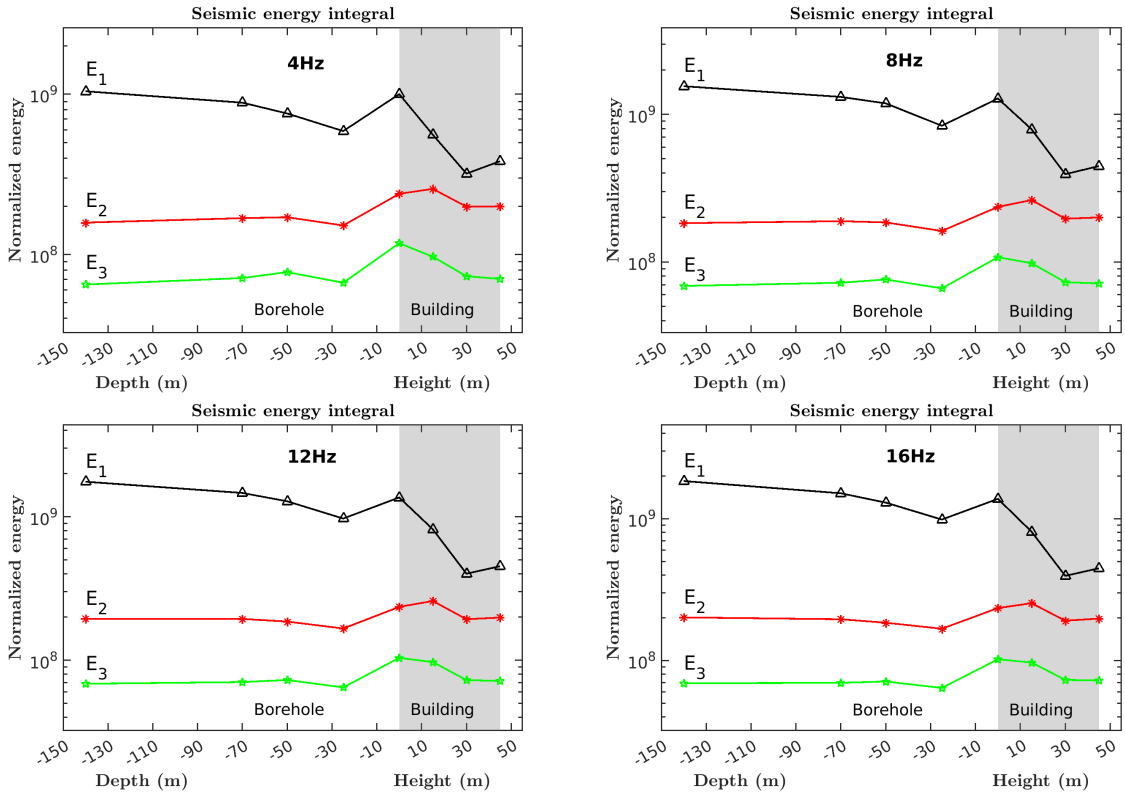

Figure 6.8: Energy integral E(r, f). The energy integrals are obtained from the seismic recording of borehole sensors and the accelerometer installed in building B22 (light shade). $\mathbf{E_1}$ (**black** solid lines), $\mathbf{E_2}$ (Red), and $\mathbf{E_3}$ (green) represent the observed energy integrals from the first, second, and third windows, respectively.

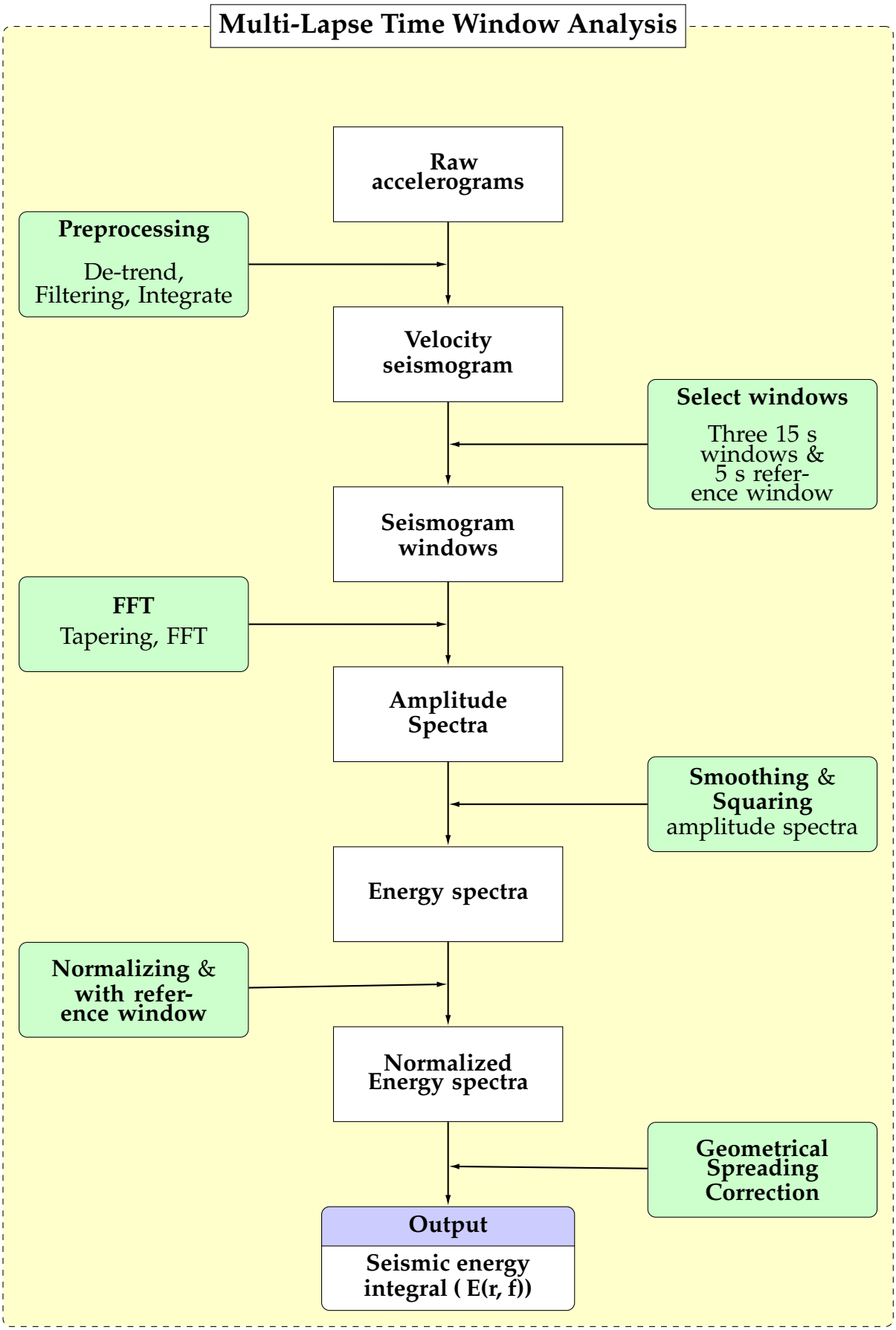

Figure 6.9: Schematic procedure for MultiLapse Time Window Analysis

The entire Multi-Lapse Time Widow analysis procedure is summarized in the flowchart in Figure 6.9.

The theoretical integral density is computed as a function of time and hypocentral distance r, E(r, t), as shown in the figure 6.10 for fitting to the observed seismic integral. E(r, t) is computed numerically using the program Hoshiba (1997) for the uniform and depth-dependent Earth model and using the analytical approximation of Paasschens (1997) for the uniform medium for comparison.

The theoretical energy integral is calculated from the time integral of three, 15 s energy density windows and a 5 s reference window as we did for the observed seismic energy integral using the equation 6.3. The geometric propagation loss is then corrected by multiplying the integrals by $4\pi r^2$.

$$E_{theo(i)}(r) = \frac{\int_{t_i}^{t_{i+1}} E(r,t)dt}{E_{ref}(r,t_{ref})} \cdot 4\pi r^2, \tag{6.3}$$

where E_{ref} is the energy estimated at the reference time interval t_{ref}.

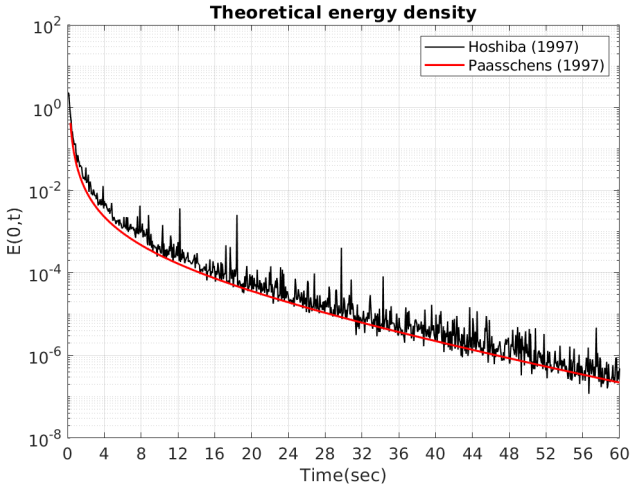

Figure 6.10: Theoretical energy density computed numerical using (Hoshiba, 1997) and using (Paasschens, 1997) analytically for half-space model.

The parameters B_0 and L_e^{-1} that simulate the theoretical energy integral that best fits the observed seismic energy are obtained by minimizing the residual or misfit function.The residual function is computed from the difference between the logarithm of the observed seismic energy and the theoretical energy integral. At site k, for a given frequency band centered at f Hz, for a pair of L_e^{-1} and B_0 values, the residual is computed from the sum of the logarithm of the energy in three windows for N events using the equation 6.4.

$$R(Le^{-1}, B_0) = \sum_{i=1}^{3}\sum_{k=1}^{N}\left\{ log_{10}(E_{obs(i)}(r_k)) - log_{10}(E_{theo(i)}(r_k, Le^{-1}, B_0)) \right\}^2 \quad (6.4)$$

where r_k is the hypo-central distance of event k.

The minimum of the function $R(L_e^{-1}, B_0)$ corresponds to the best estimate of B_0 and L_e^{-1} in the sense of least squares. Grid search and simulated annealing inversion procedures were used to minimize the misfit function. There is a computational limit to the grid search approach when the inversion involves multiple model parameters for depth dependent earth models. The use of grid search is computationally intensive but provides reliable results. To overcome the computational burden associated with the use of depth-dependent simulated annealing inversion is used. Simulated annealing dramatically reduces the computational time for inverting the observed seismic integral multilateral Earth. In some cases, the combination of grid search and simulated annealing is used for the inversion procedure.

6.2.1 Crustal attenuation estimation

6.2.1.1 MLTWA using single station

As a reference for the near-surface study attenuation, the crustal attenuation is estimated for the the Marmara region. The common procedure for estimating the crust and mantle is to use seismic data recorded from seismic stations located several tens of kilometers from the surface by multiple earthquakes.

In this study, since we have only have the seismic data records from sensors installed in one borehole and one building at a test site in the Atakoy area, we used a single-station approach of MLTWA proposed by Hoshiba (1993). Therefore, seismogram records of six earthquakes from a sensor installed at the surface (0 m) of the Atakoy borehole test site were used for MLTWA and are shown in Figure 6.11.

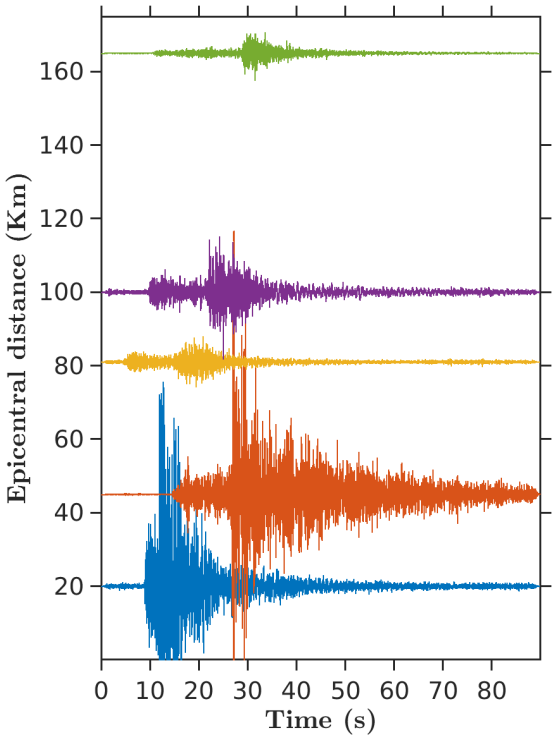

Figure 6.11: Seismograms recorded at surface station (0 m) at Atakoy borehole from six earthquakes. Note that some earthquakes appear to arrive earlier than the earthquakes near epicenter. This is because seismograms are not cut from the origin time.

The seismic energy integrals computed with MLTWA are shown in Figure 6.12. A comparison of the energy integrals E_1, E_2 and E_3 at epicentral distances from 20 km to 165 km shows that the energy from the first window E_1 decreases in value with increasing distance from the station. The observed seismic energy from the second and third windows, E_2 and E_3, respectively, are calculated from the s-coda increase in value away from the station. This observation confirms that seismic wave propagates away from the source, it encounters a lot of heterogeneity in the medium. As a result, the direct S-wave energy is converted to S-coda energy by scattering, reflection, and refraction.

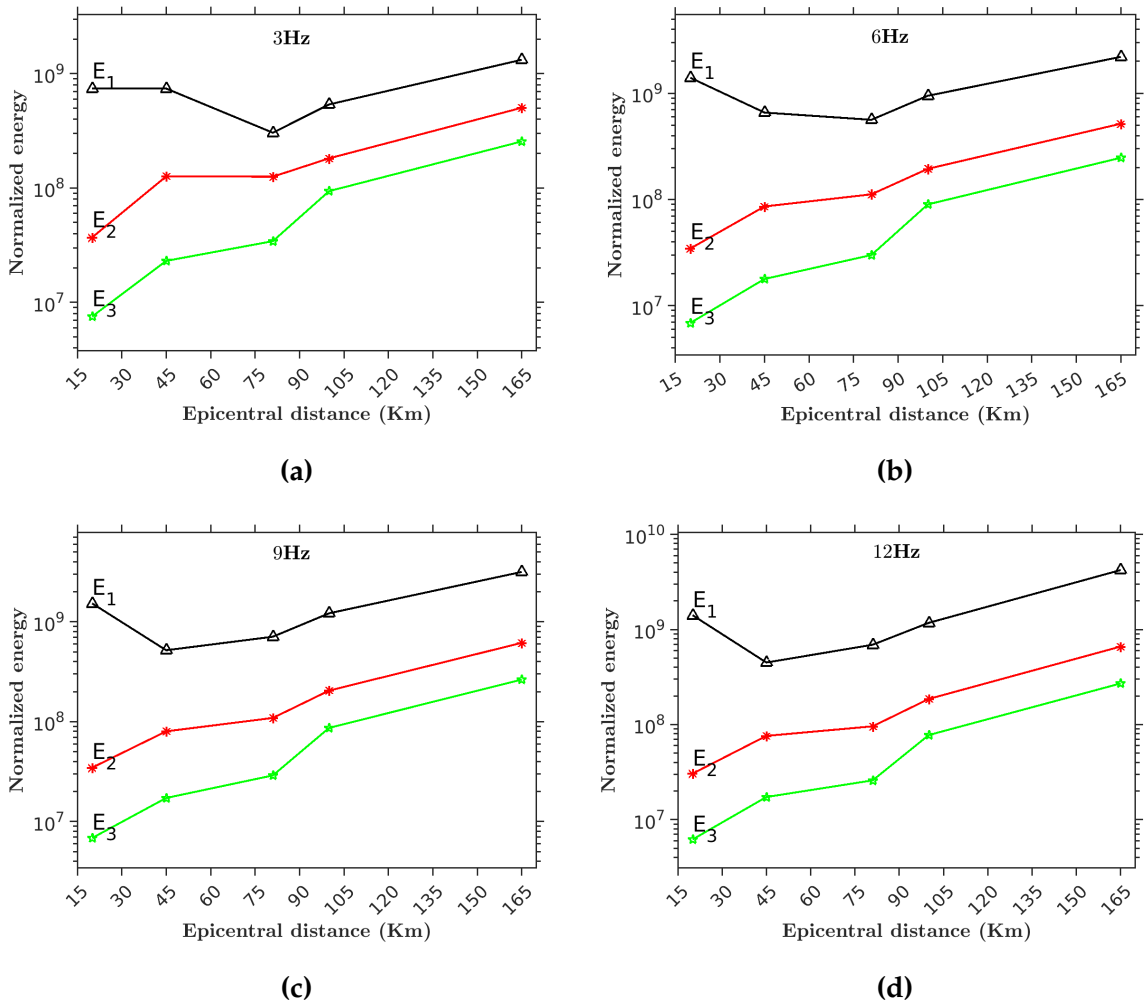

Figure 6.12: Seismic energy integrals (E(r, f)) computed at a single station from multiple earthquakes for selected frequencies of **(a)** 3 Hz, **(b)** 6 Hz, **(c)** 9 Hz and **(d)** 12 Hz. E_1 (black), E_2 (red) and E_3 (green) represent the seismic energy integrals from first, second and third window, respectively

The observed seismic energy integrals are inverted for a homogeneous half-space model using the theoretical energy density computed with Hoshiba (1997). The grid search estimates the scattering and intrinsic attenuation parameters that compute the theoretical energy density that fits the observed seismic energy integrals.

10,000 pairs of (g, h), g = n $\times$ 0.001 (n=1,...,100), h = m $\times$ 0.001 (m = 1,..., 100) for the synthetic energy were searched for the best fit. The residual is normalized to its minimum and plotted as shown in Figure 6.13a, we accepted as possible solutions those with value less than 1.1.

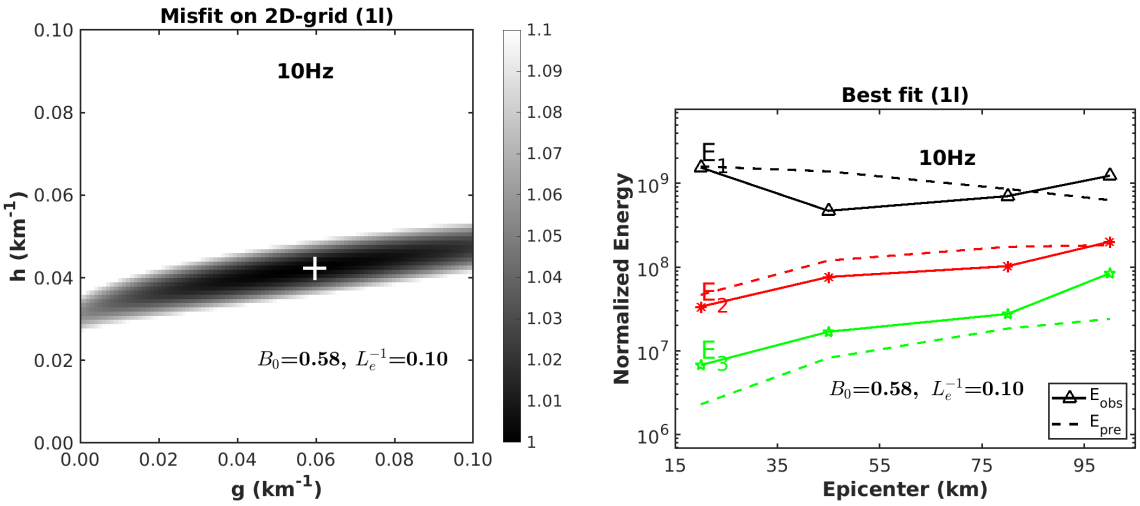

(a) **(b)**

Figure 6.13: (a) plot of normalized residual with its minimum from the result of grid search procedure. **(b)** Seismic energy integral (solid lines) & its best fit predicted energy integrals (dashed line) for B_0 and Le^{-1} pairs.

As seen in the residual plot from the grid search, (Figure 6.13a) there is a slight trade-off between the scattering (g) and intrinsic (h) attenuation coefficients, and the inversion is sensitive to the scattering attenuation coefficient. The curves in figure 6.13b don't fit well. One reason for this observation could be the use a simple(uniform) crustal model to compute the theoretical energy integral which doesn't represent the real heterogeneous crust under the test site.

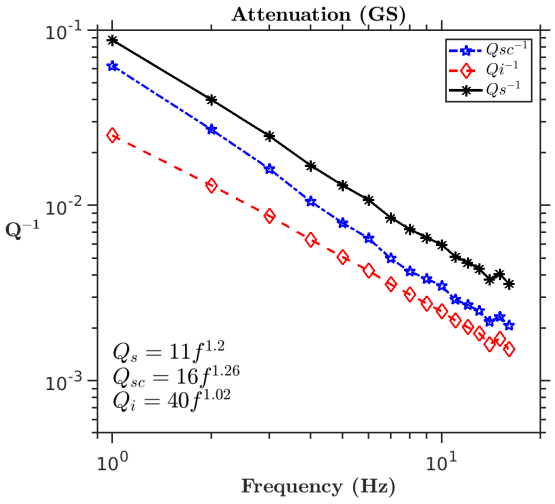

Figure 6.14: Estimated scattering (blue), intrinsic (red) and shear wave (black) attenuation values of the crust under Marmara region from the result of grid search procedure.

From the best (g) and (h) values, we estimated the quality factors for the total (Q_s), scattering (Q_{sc}), and intrinsic (Q_i) quality factors by using the following relationships:

$$Q_{sc} = \frac{2\pi f}{g.v}, \qquad Q_i = \frac{2\pi f}{h.v}, \qquad Q_s = \frac{2\pi f}{v(h+g)} \tag{6.5}$$

Fitting the values of Qs , Qsc and Qi by means of the relation $Q = Q_0 f^n$ we obtained the following attenuation relations: $Qs = 11f^{1.2}$, $Q_{sc} = 16f^{1.26}$ and $Q_i = 40f^{1.02}$.

As can be seen from the attenuation of the crust under the Atakoy test site (Fig. 6.14), the scattering attention is dominant over the intrinsic absorption. This observation could be explained by the region containing heterogeneities on the scale of the wavelength of the seismic waves, such as fractures and faults, due to its proximity to tectonic faults passing through the region.

6.2.1.2 Estimation of attenuation using vertical seismic array

Previous studies using MLTWA with seismic data used multiple stations with a separated by tens of kilometers from multiple local and regional earthquakes. They used these data to estimate the attenuation of the crust and upper mantle of a region under study.

This study estimates the near-surface scattering and intrinsic absorption for shear waves in the subsurface of Ataköy, Istanbul, Turkey, and of a nearby building. The seismograms used for the study is are recorded by down-hole seismic arrays from sensors deployed in four boreholes and accelerograms were installed at different heights on a building about 50 m from the boreholes as shown in Figure 6.1a at the Ataköy test site.

As can be seen from the seismogram recordings (Figure 6.15), the amplitude of the seismograms increases from the deepest sensor (140 m) towards the surface. This is explained

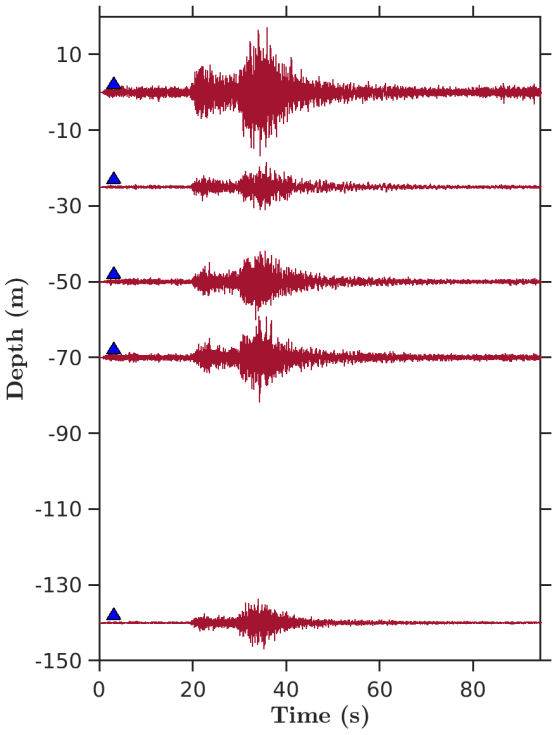

Figure 6.15: Seismograms recorded from the vertical array of sensors installed borehole at, Atakoy test site for 2013 Istanbul earthquake.

by the decrease in impedance towards the surface.

The attenuation of the crust under the study area (Marmara region) is estimated using grid search (Fig. 6.16) and simulated annealing inversion (Fig. 6.18) to compare the two inversion approaches. A total of 2500 pairs of (g, h), g = n $\times$ 0.03 (n=1,...,50), h = m $\times$ 0.01 (m = 1,..., 50) for the synthetic energy were searched for the best fit.

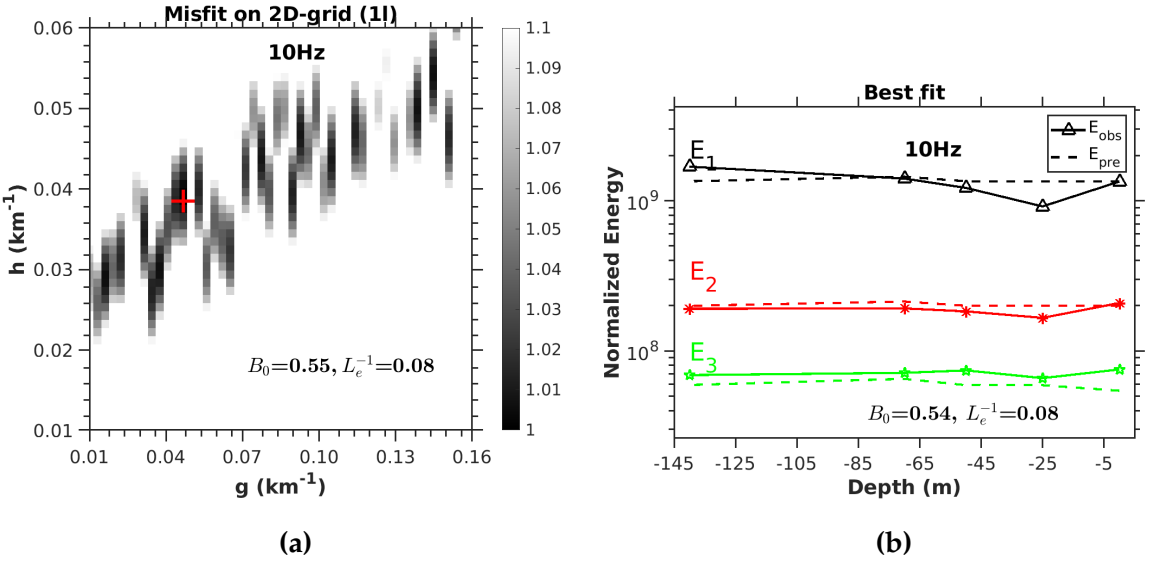

(a) **(b)**

Figure 6.16: **(a)** Normalized residual from grid search result. The red plus sign represents the minimum. **(b)** Seismic energy integral (from vertical array) predicted energy integral best-fit

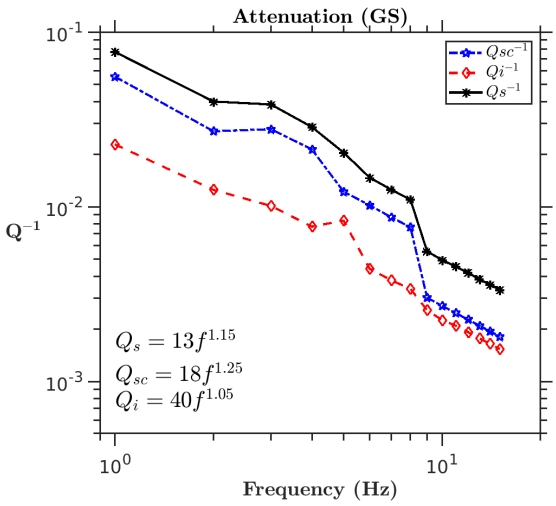

Figure 6.17: Estimated scattering and intrinsic attenuation using a grid search procedure for a vertical seismic array.

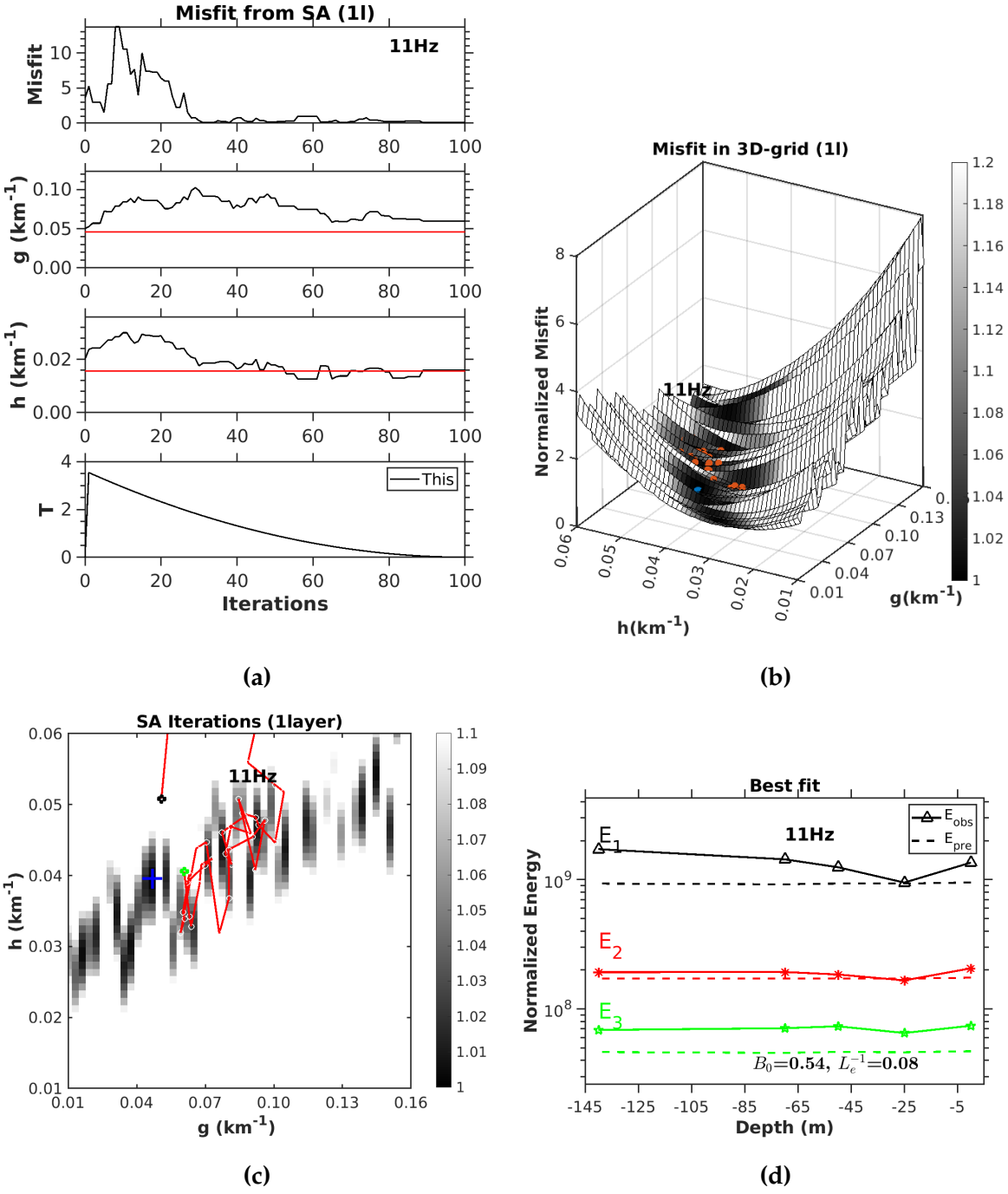

Figure 6.18: Results of simulated annealing inversion procedure. **(a)** Plot of residual (top) and model parameters g (2nd row) and h (third row) as a function of iteration number. **(b)** 3D plot of the residual as a function of the attenuation coefficients. **(c)** Error surface (colors), showing true solution (green circle),and a series of solutions (white circles) connected by red lines. **(d)** Seismic energy integrals with corresponding best-fitted energy integral.

The estimated scattering, intrinsic, and total shear wave attenuations are shown in Fig. 6.17. The relative contribution of the scattering attenuation is larger than the intrinsic absorption, similar to the estimation using the single-station approach (Fig. 6.14). This is observed at for the entire frequency range of 1-15 Hz.

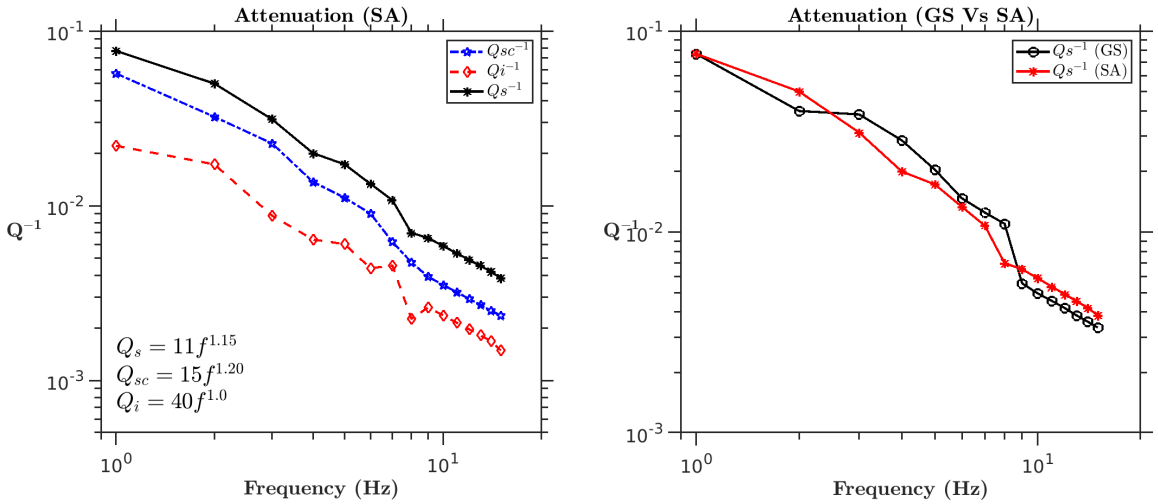

(a) **(b)**

Figure 6.19: (a) Estimated attenuation using simulated annealing inversion. **(b)** Comparison of attenuation result from the grid search (black solid line) and simulated annealing inversion (red solid ine)

The figure 6.19b compares the attenuation results of from the grid search and the simulated annealing inversion. As can be seen from the plot in Figure 6.19b, the results from the two inversion methods are comparable.

6.2.2 Attenuation in depth-dependent model using a vertical array of seismograms

Since a non-uniform distribution of scatterers is more realistic than using a uniform earth model, depth dependent earth model is applied to estimate the attenuation parameters. This study estimates, the near-surface scattering and intrinsic absorption for shear waves in the subsurface of Ataköy, Istanbul, Turkey, and a nearby building. The intrinsic and scattering attenuations are estimated using a uniform half-space and a more realistic depth-dependent earth media model over a frequency range of 1 to 15 Hz. For example, the shear wave attenuatio estimation through a building is estimated by assuming that the building is a horizontal layer over a half-space (the underlying ground).

6.2.3 Attenuation through building (B22)

Four accelerometers are installed in the B22 building under study, and the seismogram recordings are shown in Figure 6.20. The amplitude of the seismograms increases from the bottom floor the upward to the top floor due to the vibration of the building.

Building "B22" has a height of 46.65 m, including 4.0 m in the basement from the foundation to the roof, excluding the elevator machine room at the top. The building has 20 cm thick concrete interior walls as part of the structure, except for the elevator shaft walls which are 15 cm thick. Floor slabs are 16 cm thick. The exterior walls are precast concrete panels.

Petrovic et al. (2018) estimated an average shear wave velocity of 320 m/s through the building using deconvolution interferometry. The materials from which the building is constructed have a density of 2.0 g/cm^3. These parameters are used in the input model to simulate the theoretical energy density for the inversion.

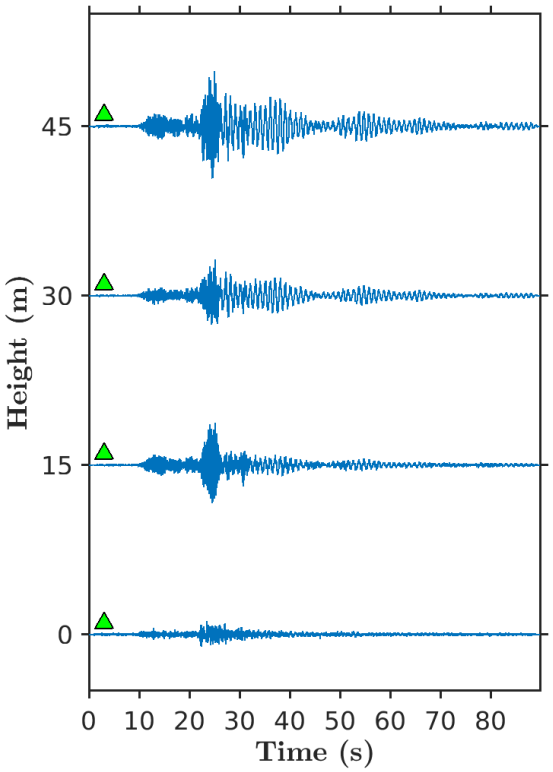

Figure 6.20: Vertical array of seismograms recorded from sensors installed o n building 'B22', at Atakoy test from 2015 Istanbul earthquake. Blue triangle are the sensors position on the building.

In order to estimate a realistic attenuation value through the building, we assumed the building as a flat layer over a half-space(the lower surface). Intrinsic and scattering attenuation is estimated through the building using a grid search approach for the frequency range of 1 to 16 Hz.

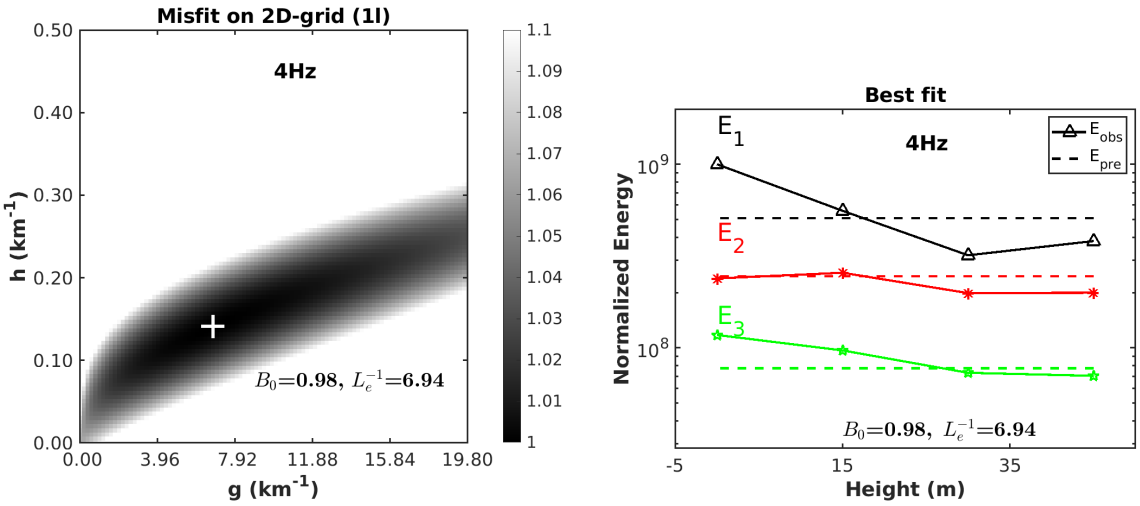

(a) (b)

Figure 6.21: (a) Normalized residual from grid search result. **(b)** Seismic energy(from vertical array of seismograms on the building) with the best-fit predicted energy

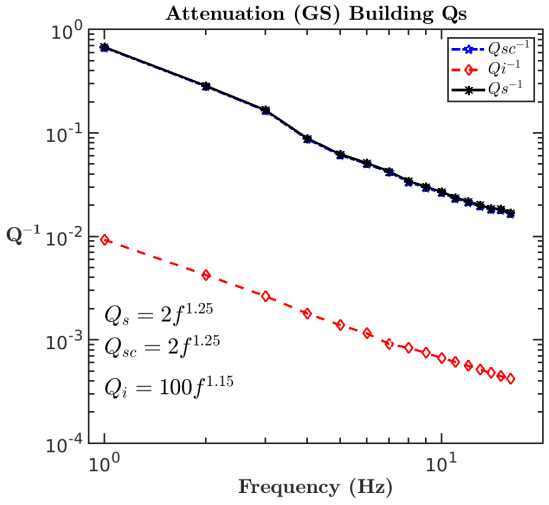

Figure 6.22: Estimated attenuation of inside reinforced concrete building B22.

The scattering attenuation contributes significantly to the total shear wave attenuation. This could be explained by the large s-coda amplitude of the seismograms recorded at the building. The s-coda amplitudes at the building, unlike those seismograms in the borehole seismograms, do not consist entirely of scattered waves; they are partly contributed by the vibration of the building. Therefore, the attenuation result of the at the building is biased.

6.2.3.1 Near-surface attenuation

The attenuation for depth depends on a layer (50 m deep from the surface) and a half-space below the first layer. The attenuation coefficients that characterize the model are h_1 and g_1 for the first layer, and h_2 and g_2 for the half-space below.

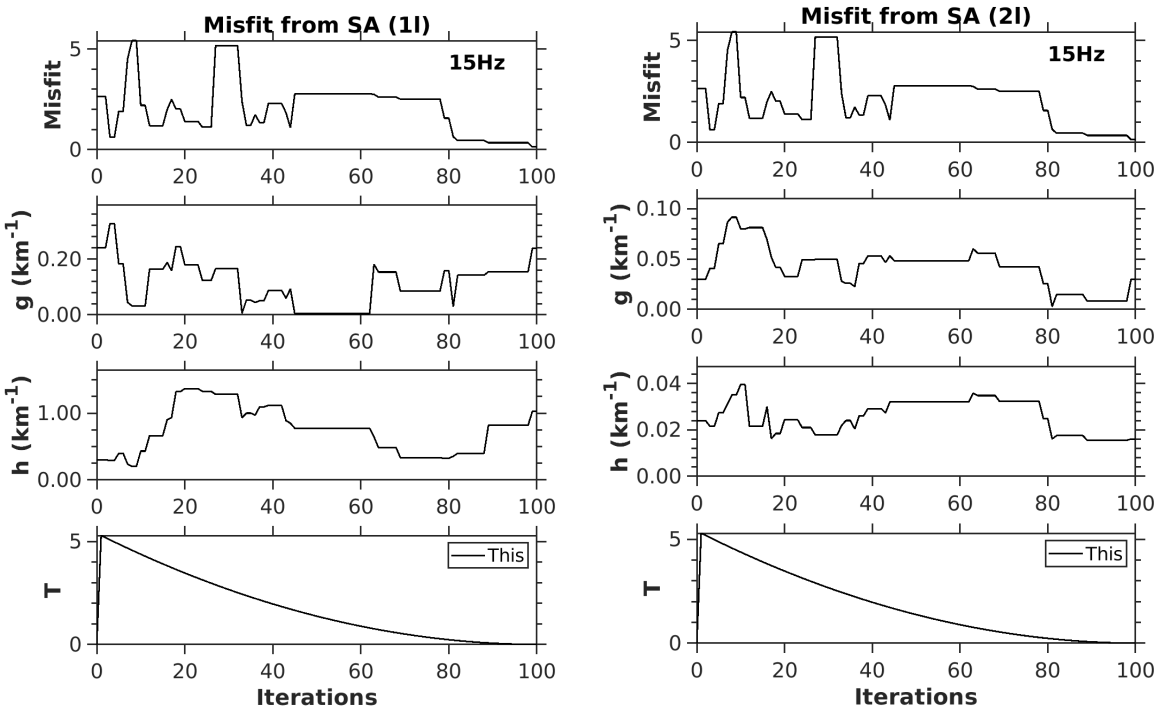

(a) **(b)**

Figure 6.23: Simulated annealing inversion results for depth dependent model. **(a)** Residual(top) and g and h as a function of iteration for 1st layer. **(b)** Residual(top) g and h as a function of iteration for the 2nd layer.

As the number of parameters increases, the grid search approach becomes impractical due to large computational requirements. Therefore, the simulated annealing inversion approach is used for the depth-dependent near model.

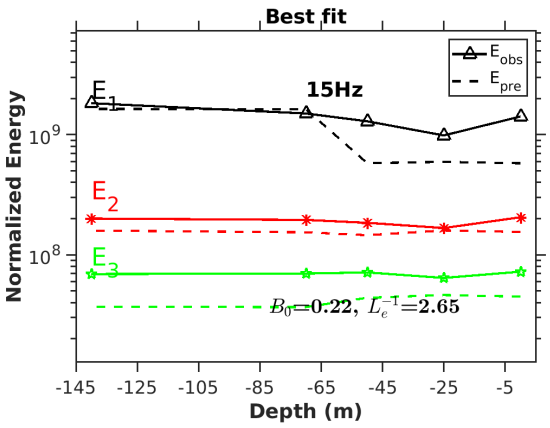

Figure 6.24: Seismic energy integral with its best fitted predicted energy.

Figure 6.24 shows the best fit of the observed energy integral (solid lines) with the theoretical energy integral (dashed lines) of the two-layer Earth model. The two lines are better fitted here than for the uniform half-space model because the two-layer Earth model is a more realistic representation of the Earth's crust , resulting in the observed seismic energy integrals.

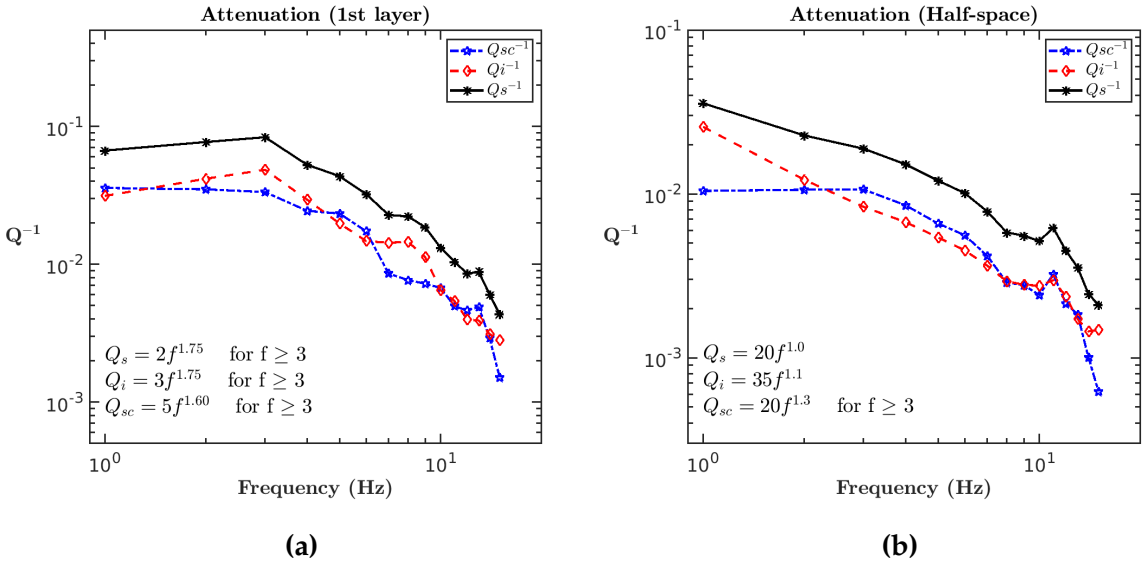

(a) **(b)**

Figure 6.25: Estimated attenuation for depth-dependent model using simulated annealing inversion. **(a)** Estimated attenuation for a 50 m shallow layer. **(b)** Estimated attenuation for half-space layer below 50 m

Figure 6.25 compares the shear wave attenuation through the a shallow layer of 50 m thickness and the half-space (crust) below. Comparing the total shear wave attenuation between the two layers, the attenuation in the first layer is higher than the second (deeper) layer. This is also observed in the near-surface attenuation studies by Dikmen et al. (2016) and Parolai et al. (2010) over the Atakoy test site.

Chapter 7

Discussion of the results

7.1 Attenuation of half-space (uniform model)

According to several authors such Akinci et al. (2020) strong frequency dependence could be related to the size of the heterogeneities. In such a hypothesis, a strong frequency dependence of Qs^{-1} occurs when the heterogeneities responsible for the scattering are, at least, comparable to the the wavelength for the lowest frequencies analyzed (about 2 km).

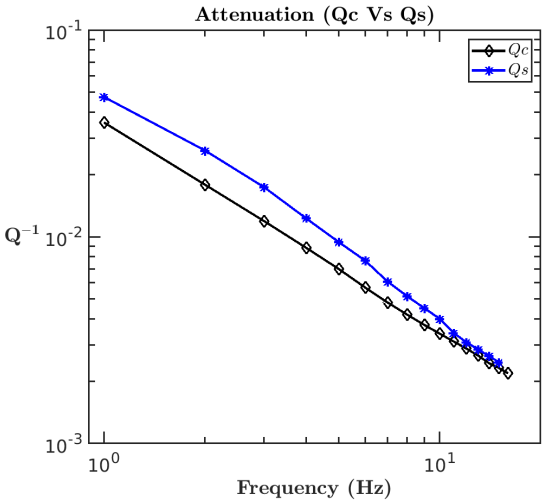

Figure 7.1: Shear wave attenuation estimated for the crust below Marmara region using MLTWA and coda attenuation using coda method.

The shear wave attenuation is estimated for the crust beneath the Marmara region using a uniform half-space model. From our result we that obtained that Qs values ranging from 21 at 1 Hz and up to 404 at 15 Hz. In addition, we observed that the

scattering attenuation dominates over the intrinsic dissipation in all the frequency bands.

The coda attenuation is estimated from the coda envelope of the seismogram recorded by, the sensors installed borehole estimate for the same region using the coda method to compare it with our results shear wave attenuation. The comparison of the two methods is then shown in the figure 7.1. The results of the two methods are comparable. This could be a way to verify the validity of the method we used to estimate the shear wave attenuation.

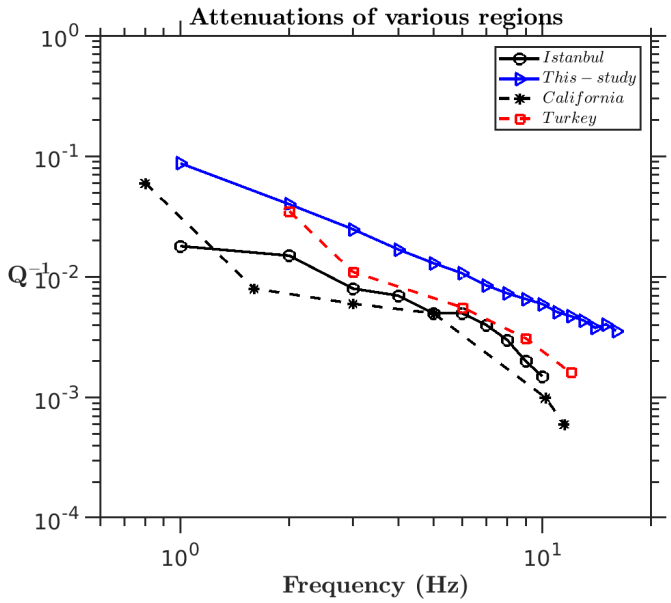

Figure 7.2: Comparison of the Qs^{-1} versus frequency for different regions: Istanbul (Bindi et al., 2006); California (Jin et al., 1994); Turkey (Akinci and Eyidoğan, 2000).

Shear wave attenuation of the Marmara region is presented with attenuation studies around Turkey is shown in Figure 7.2 for comparison.

7.2 Estimation of near-surface (depth dependent) attenuation

The important part of this study, is the separate estimation of scattering attenuation and intrinsic absorption using a depth dependent model inside a building and for the near surface geology beneath the Atakoy test site.

The shear wave attenuation through the three layers is shown in Figure 7.3 for comparison. The shear wave attenuation through a building (46 m high), a shallow layer of 50 m thickness below the building, and the crust (half-space model) decreases with

increasing depth from the surface.

When comparing the attenuation obtained in a layer and a half-space, the attenuation due to both scattering and intrinsic absorption in the first layer is more significant than the values in the half-space below. For example, at 5 Hz, the estimated shear wave quality factor (Qs) in the building, the near-surface layer (50 m thick) and the half-space are 16, 23, and 83, respectively. These results are in agreement with Dikmen et al. (2016) and Parolai et al. (2010) estimation of the Qs values on the same test site. Parolai et al. (2010) estimated an average of 30, 46, and 99 for the 0 - 50, 0 - 70, and 0 - 140 m depth ranges, respectively, using spectral fitting for the 1-15 Hz frequency band. In addition, Hutchings and Viegas (2012) also estimated estimated Qs value of between 10 and 100 for near-surface geology. Therefore, our estimate is in a good agreement with these previous studies.

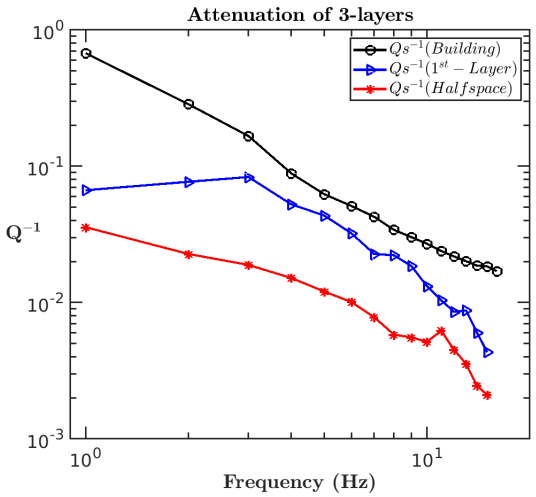

Figure 7.3: Attenuation (Qs^{-1}) of building and two-layers underneath the building.

In this study, attenuation is observed to decrease with depth. The comparison of attenuation layered media in this study reinforces the widely accepted observation which is that heterogeneity decreases with increasing depth as demonstrated by Hoshiba (1997), Hoshiba et al. (2001), and Giampiccolo et al. (2006). We found that the attenuation due to scattering and intrinsic absorption is more significant in the first layer than in the underlying half-space. Therefore, using the non-uniform distribution of scatterers is more realistic than a uniform earth model and, as a result, the attenuation decreases with depth.

Chapter 8

Conclusion

Separate estimation of the attenuation due intrinsic absorption and scattering in near-surface geology and built-in structures is essential in engineering seismology. Knowledge of intrinsic absorption and scattering attenuation parameters could be used for site response studies; and prediction of strong motions in engineering seismology for seismic hazard and risk studies. In addition, knowledge of the structures of intrinsic and scattering attenuation provides insight into the nature of the Earth's interior and imposes constraints on seismic wave propagation. Therefore, the ability to separately estimate the spatial distributions of intrinsic (Q_i^{-1}) and scattering (Q_{sc}^{-1}) attenuation is crucial for improving our understanding of the wave propagation through near-surface geology and built-in structures.

In this study, two methods were used in this study to estimate the intrinsic and scattering attenuation parameters: the coda method to estimate the coda quality factor for the uniform half-space model and the Multi-Lapse Time Window Analysis (MLTWA) to separately estimate intrinsic (Q_i^{-1}) and scattering (Q_{sc}^{-1}) attenuation for uniform half-space model for a more realistic depth-dependent earth media model.

This study attempted to estimate the intrinsic (Q_i^{-1}) and scattering (Q_{sc}^{-1}) attenuation using seismic data collected from sensors installed in a borehole and a nearby building test site in Atakoy, Istanbul, Turkey.

In this study, two methods were used in this study to estimate the intrinsic and scattering attenuation parameter:

1) The **coda method** is used to estimate the coda quality factor for the uniform half-space model. For a source co-located with a receiver, the shape of the time-domain S-coda envelope filtered at a given frequency and the band centered at f can be explained by the exponential decay of the equation $A(f,t) \propto \frac{1}{t^n} e^{-\frac{\pi f t}{Q_c(f)}}$. Then coda attenuation ($Q_c^{-1}(f)$) is estimated from recorded seismograms by fitting the envelopes of the band-pass filtered seismic traces to $A(f,t) \propto \frac{1}{t^n} e^{-\frac{\pi f t}{Q_c(f)}}$. Using coda method the

($Q_c^{-1}(f)$) for the crust below the Marmara region, turkey is estimated using uniform half-space model.

2) The **Multi-Lapse Time Window Analysis (MLTWA)** method is used to separately estimate intrinsic (Q_i^{-1}) and scattering (Q_{sc}^{-1}) attenuation for uniform half-space model for a more realistic depth-dependent earth media model. MLTWA compares the seismic energy integrated from three consecutive seismic windows starting from the S-wave arrival time and plotted against hypo-central distance, with the energy integrals predicted by a theoretical model suitable for the multiple scattering problem. The theoretical energy envelopes computed numerically using Hoshiba (1997) (which uses a Monte Carlo approach)for the depth-dependent model. In addition this study developed an innovative approach by modifying the MLTWA method to use a vertical array of seismograms to separately estimate the scattering and intrinsic seismic attenuation of depth dependent near-surface media and buildings.

Since the application of MLTWA to a depth dependent medium model,is computationally demanding, an inversion strategy combining grid search and simulated annealing is applied. Grid Search is used over a wide range of parameter space, but with a relatively large grid spacing, to find possible narrow parameter spaces with a potential solution. We use the narrowed parameter space identified by the Grid Search to constrain our region of the search space of the solution using simulated Annealing. Simulated Annealing converges to the solution in a few of hundred iterations or sometimes less which much faster that the Grid Search approach.

MLTWA method is applied to estimate the intrinsic and scattering shear wave attenuation is estimated for a building and two layers in the near surface beneath the building. Frequency dependent Q_i, Q_{sc}, and Q_s values are estimated for frequencies from 1 to 15 Hz. Qs values $Q_s = 2f^{1.25}$, $Q_s = 2f^{1.75}$ and $Q_s = 20f^{1.0}$ are estimated for the building, the first layer and the half-space below respectively.Finally the estimated results fro uniform half space model from coda method MLTWA is compared with each other.

Comparing the scattering attenuation for different layers obtained from this study, we found that the scattering attenuation decreases with depth towards the deeper layer. In general, this effect could be explained by a decrease in the heterogeneity of the medium as we go deeper from the surface.

Finally result of the estimated near-surface shear wave attenuation values can applied for site response studies and for predicting strong motions in engineering seismology for seismic hazard and risk studies. In addition, the result of the scattering and intrinsic attenuation estimation could be important to study the heterogeneity of the underlying medium. Estimated intrinsic attenuation values could be applied in exploration geophysics to study geothermal reservoirs. A high intrinsic attenuation value could indicate whether a region is saturated with water or not.

8.1 Limitations of the study

The following are some limitation of the MLTWA method observed during the study:

A slight trade-off between the scattering and intrinsic attenuation parameters is observed during the inversion process in our efforts to estimate the scattering and intrinsic of the attenuation parameters separately.

The use of MLTWA for the depth-dependent earth model results in a huge computational demand during the inversion process, so it was not possible to estimate the scattering and attenuation parameters for more than three layers. The computation time increases when using the MLTWA for shallow (low velocity) thin layers. However, it is possible to use this approach to estimate attenuation through multiple layers, using a more robust computational facility.

In the future I will further develop the methodology to use it for separate estimation of the intrinsic and scattering attenuation in multi-layered depth-dependent shallow crust and attenuation in buildings using more robust computational facility such as hyper performance computing (HPC).

Bibliography

Abdel-Fattah, Ali K et al. (2008). "Intrinsic and scattering attenuation in the crust of the Abu Dabbab area in the eastern desert of Egypt". In: *Physics of the Earth and Planetary Interiors* 168.1-2, pp. 103–112.

Aki, K (1969). "Analysis of the seismic coda of local earthquakes as scattered waves". In: *Journal of geophysical research* 74.2, pp. 615–631.

— (1980). "Attenuation of shear-waves in the lithosphere for frequencies from 0.05 to 25 Hz". In: *Physics of the Earth and Planetary Interiors* 21.1, pp. 50–60.

Aki, K and B Chouet (1975). "Origin of coda waves: source, attenuation, and scattering effects". In: *Journal of geophysical research* 80.23, pp. 3322–3342.

Akinci, Aybige, Edoardo Del Pezzo, and Luca Malagnini (2020). "Intrinsic and scattering seismic wave attenuation in the Central Apennines (Italy)". In: *Physics of the Earth and Planetary Interiors* 303, p. 106498.

Akinci, Aybige and Haluk Eyidoğan (2000). "Scattering and anelastic attenuation of seismic energy in the vicinity of north Anatolian fault zone, eastern Turkey". In: *Physics of the Earth and Planetary Interiors* 122.3-4, pp. 229–239.

Bianco, F et al. (2005). "Separation of depth-dependent intrinsic and scattering seismic attenuation in the northeastern sector of the Italian Peninsula". In: *Geophysical Journal International* 161.1, pp. 130–142.

Bindi, Dino et al. (2006). "Crustal attenuation characteristics in northwestern Turkey in the range from 1 to 10 Hz". In: *Bulletin of the Seismological Society of America* 96.1, pp. 200–214.

Chouet, Bernard (1990). "Effect of anelastic and scattering structures of the lithosphere on the shape of local earthquake coda". In: *pure and applied geophysics* 132.1, pp. 289–310.

Dikmen, S Umit, Ali Pinar, and Ayse Edincliler (2016). "Near-surface attenuation using traffic-induced seismic noise at a downhole array". In: *Journal of Seismology* 20, pp. 375–384.

Fehler, M et al. (1992). "Separation of scattering and intrinsic attenuation for the Kanto-Toka region, Japan, using measurements of S-wave energy versus hypocentral distance". In: *Geophysical Journal International* 108.3, pp. 787–800.

Filippucci, Marilena et al. (2021). "Seismic Envelopes of Coda Decay for Q-coda Attenuation Studies of the Gargano Promontory (Southern Italy) and Surrounding Regions". In: *Data* 6.9, p. 98.

Frankel, A and Leif Wennerberg (1987). "Energy-flux model of seismic coda: separation of scattering and intrinsic attenuation". In: *Bulletin of the Seismological Society of America* 77.4, pp. 1223–1251.

Gao, LS et al. (1983). "Effects of multiple scattering on coda waves in three-dimensional medium". In: *pure and applied geophysics* 121.1, pp. 3–15.

Giampiccolo, E et al. (2006). "S-waves attenuation and separation of scattering and intrinsic absorption of seismic energy in southeastern Sicily (Italy)". In: *Geophysical Journal International* 165.1, pp. 211–222.

Gill, Philip E et al. (1981). "Aspects of mathematical modeling related to optimization". In: *Applied Mathematical Modelling* 5.2, pp. 71–83.

Hoshiba, Mitsuyuki (1991). "Simulation of multiple-scattered coda wave excitation based on the energy conservation law". In: *Physics of the Earth and Planetary Interiors* 67.1-2, pp. 123–136.

— (1993). "Separation of scattering attenuation and intrinsic absorption in Japan using the multiple lapse time window analysis of full seismogram envelope". In: *Journal of Geophysical Research: Solid Earth* 98.B9, pp. 15809–15824.

— (1997). "Seismic coda wave envelope in depth-dependent S wave velocity structure". In: *Physics of the Earth and Planetary Interiors* 104.1-3, pp. 15–22.

Hoshiba, Mitsuyuki et al. (2001). "Scattering attenuation and intrinsic absorption using uniform and depth-dependent model–Application to full seismogram envelope recorded in Northern Chile". In: *Journal of seismology* 5, pp. 157–179.

Hutchings, Lawrence and Gisela Viegas (2012). "Application of empirical Green's functions in earthquake source, wave propagation and strong ground motion studies". In: *Earthquake Research and Analysis-New Frontiers in Seismology*, pp. 87–140.

Jacobsen, RS (1987). "An investigation into the fundamental relationship between attenuation, phase dispersion, and frequency using seismic refraction profiles over sedimentary structures". In: *Geophysics* 52.1, pp. 72–87.

Jin, Anshu et al. (1994). "Separation of intrinsic and scattering attenuation in southern California using TERRAscope data". In: *Journal of Geophysical Research: Solid Earth* 99.B9, pp. 17835–17848.

Kikuchi, Masayuki (1981). "Dispersion and attenuation of elastic waves due to multiple scattering from cracks". In: *Physics of the Earth and Planetary Interiors* 27.2, pp. 100–105.

Kim, Jun Kyoung et al. (2017). "Amplification characteristics of seismic observation sites from S-wave energy, coda waves, and background noise from the Fukuoka earthquake series". In: *Exploration Geophysics* 48.3, pp. 264–271.

Kirkpatrick (1983). "Optimization by simulated annealing". In: *science* 220.4598, pp. 671–680.

Knopoff, L and JA Hudson (1964). "Scattering of elastic waves by small inhomogeneities". In: *The Journal of the Acoustical Society of America* 36.2, pp. 338–343.

Konno, Katsuaki and Tatsuo Ohmachi (1998). "Ground-motion characteristics estimated from spectral ratio between horizontal and vertical components of microtremor". In: *Bulletin of the Seismological Society of America* 88.1, pp. 228–241.

Kopnichev, Yu F (1977). "The role of multiple scattering in the formation of seismogram's tail". In: *Izv. Akad. Nauk SSSR, Fiz. Zem.* 13, pp. 394–398.

Lore.trango (2010). *Seismic attenuation*. https://commons.wikimedia.org/wiki/File:Seismic_attenuation_body_surface_waves.png.

Menke, W (2012). "Geophysical data analysis: discrete inverse theory, MATLAB edn". In: *New York: Academic*.

O'Connell, Richard J and Bernard Budiansky (1977). "Viscoelastic properties of fluid-saturated cracked solids". In: *Journal of Geophysical Research* 82.36, pp. 5719–5735.

Odziemczyk, Waldemar (2020). "Application of simulated annealing algorithm for 3D coordinate transformation problem solution". In: *Open Geosciences* 12.1, pp. 491–502.

Paasschens, JCJ (1997). "Solution of the time-dependent Boltzmann equation". In: *Physical Review E* 56.1, p. 1135.

Parolai, S. (2012). "Investigation of site response in urban areas by using earthquake data and seismic noise". In: *New manual of seismological observatory practice 2 (NMSOP-2)*. Deutsches geoforschungszentrum gfz, pp. 1–38.

— (2018). "κ_0: Origin and usability". In: *Bulletin of the Seismological Society of America* 108.6, pp. 3446–3456.

Parolai, S., D. Bindi, and M. Pilz (2015). "k0: The role of Intrinsic and Scattering Attenuation". In: *Bulletin of the Seismological Society of America* 105.2A, pp. 1049–1052.

Parolai, S et al. (2009). "The Ataköy vertical array (Turkey): insights into seismic wave propagation in the shallow-most crustal layers by waveform deconvolution". In: *Geophysical Journal International* 178.3, pp. 1649–1662.

Parolai, S. et al. (2010). "Determination of shallow S-wave attenuation by down-hole waveform deconvolution: a case study in Istanbul (Turkey)". In: *Geophysical Journal International* 181.B9, pp. 1147–1158.

Petrovic, B, S Umit Dikmen, and Stefano Parolai (2018). "Real data and numerical simulations-based approaches for estimating the dynamic characteristics of a tunnel formwork building". In: *Bulletin of Earthquake Engineering* 16, pp. 1633–1656.

Petrovic, B et al. (2018). "Joint deconvolution of building and downhole seismic recordings: an application to three test cases". In: *Bulletin of Earthquake Engineering* 16, pp. 613–641.

Rautian, TG and VI Khalturin (1978). "The use of the coda for determination of the earthquake source spectrum". In: *Bulletin of the Seismological Society of America* 68.4, pp. 923–948.

Sato, H (1993). "Energy transportation in one-and two-dimensional scattering media: analytic solutions of the multiple isotropic scattering model". In: *Geophysical Journal International* 112.1, pp. 141–146.

Sato, H and M Fehler (1998). "Seismic Wave Propagation and Scattering in the Heterogeneous Earth. Springer-Verlag, New York, 308 p". In.

Sato, Haruo, Michael C Fehler, and Takuto Maeda (2012). *Seismic wave propagation and scattering in the heterogeneous earth*. Springer Science and Business Media.

Sen, Mrinal K and Paul L Stoffa (2013). *Global optimization methods in geophysical inversion*. Cambridge University Press.

Sharma, Babita, Himanshu Mittal, and Arjun Kumar (Mar. 2015). "A Reappraisal of Attenuation of Seismic Waves and its relevance towards Seismic Hazard". In: *International Journal of Advanced Research* 3, pp. 296–305.

Shiomi, Katsuhiko, Haruo Sato, and Masakazu Ohtake (1997). "Broad-band power-law spectra of well-log data in Japan". In: *Geophysical Journal International* 130.1, pp. 57–64.

Sørensen, Mathilde B et al. (2006). "Local site effects in Ataköy, Istanbul, Turkey, due to a future large earthquake in the Marmara Sea". In: *Geophysical Journal International* 167.3, pp. 1413–1424.

Stein, Seth and Michael Wysession (2009). *An introduction to seismology, earthquakes, and earth structure*. John Wiley and Sons.

Taylor, Steven R, Brian P Bonner, and George Zandt (1986). "Attenuation and scattering of broadband P and S waves across North America". In: *Journal of Geophysical Research: Solid Earth* 91.B7, pp. 7309–7325.

Vargas, Carlos A et al. (2004). "Spatial variation of coda wave attenuation in northwestern Colombia". In: *Geophysical Journal International* 158.2, pp. 609–624.

Wesley, James Paul (1965). "Diffusion of seismic energy in the near range". In: *Journal of geophysical research* 70.20, pp. 5099–5106.

Wu, Ru-Shan and K. Aki (1985). "Multiple Scattering and Energy Transfer of Seismic Waves Separation of Scattering Effect from Intrinsic Attenuation II. Application of the Theory to Hindu Kush Region". In: *PAGEOPH* 128.1/2, p. 198.

— (1988). "Introduction: Seismic wave scattering in three-dimensionally heterogeneous earth". In: *Scattering and attenuations of seismic waves, Part I*, pp. 1–6.

Zeng, Y., F. Su, and K. Aki (1991). "Scattering wave energy propagation in a random isotropic scattering medium: 1. Theory". In: *Journal of Geophysical Research: Solid Earth* 96.B1, pp. 607–619.

Appendix A

Theoretical energy density

Paasschens (1997) provided the approximate analytical solution in 3-D space, assuming an infinite half-space with constant characteristics and isotropic scattering, which is represented as follows:

$$E(r,t) \approx \frac{We^{-g_0 V_0 t}}{4\pi V_0 r^2}\delta\left(t-\frac{r}{V_0}\right) + W\frac{(1-r^2/(V_0 t)^2)^{1/8}}{(4\pi V_0 t/(3V_0))^{3/2}}e^{-g_0 V_0 t}M\left(g_0 V_0 t(1-\left(\frac{r^2}{V_0^2 t^2}\right)^{3/4}\right)H(t-\frac{r}{V_0}) \quad \text{(A.1)}$$

and

$$M(x) \simeq e^x\sqrt{(1+2.026/x)}$$

where E(r,t) is the energy density, r is hypo-central distance, t is lapse time from the origin time, f is frequency, v is seismic wave velocity (assumed constant), δ is the Dirac function, H is the Heaveside unit step function, g(z) is scattering coefficient, and h(z) represents the intrinsic absorption strength respectively,

Appendix B

Best fit energy from single station

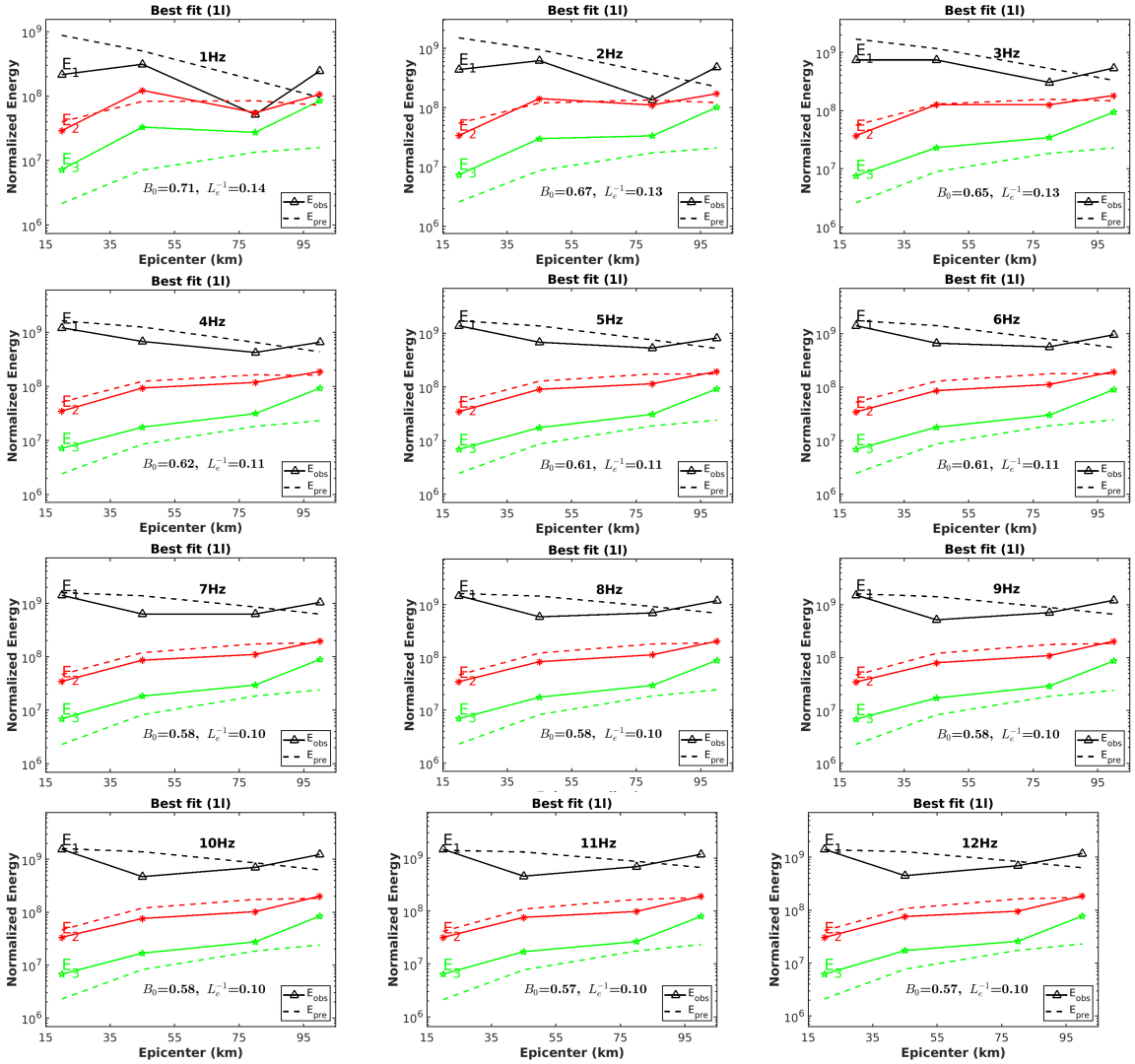

Figure B.1: Bestfit energy

Appendix C

Best-fit energy from half-space model

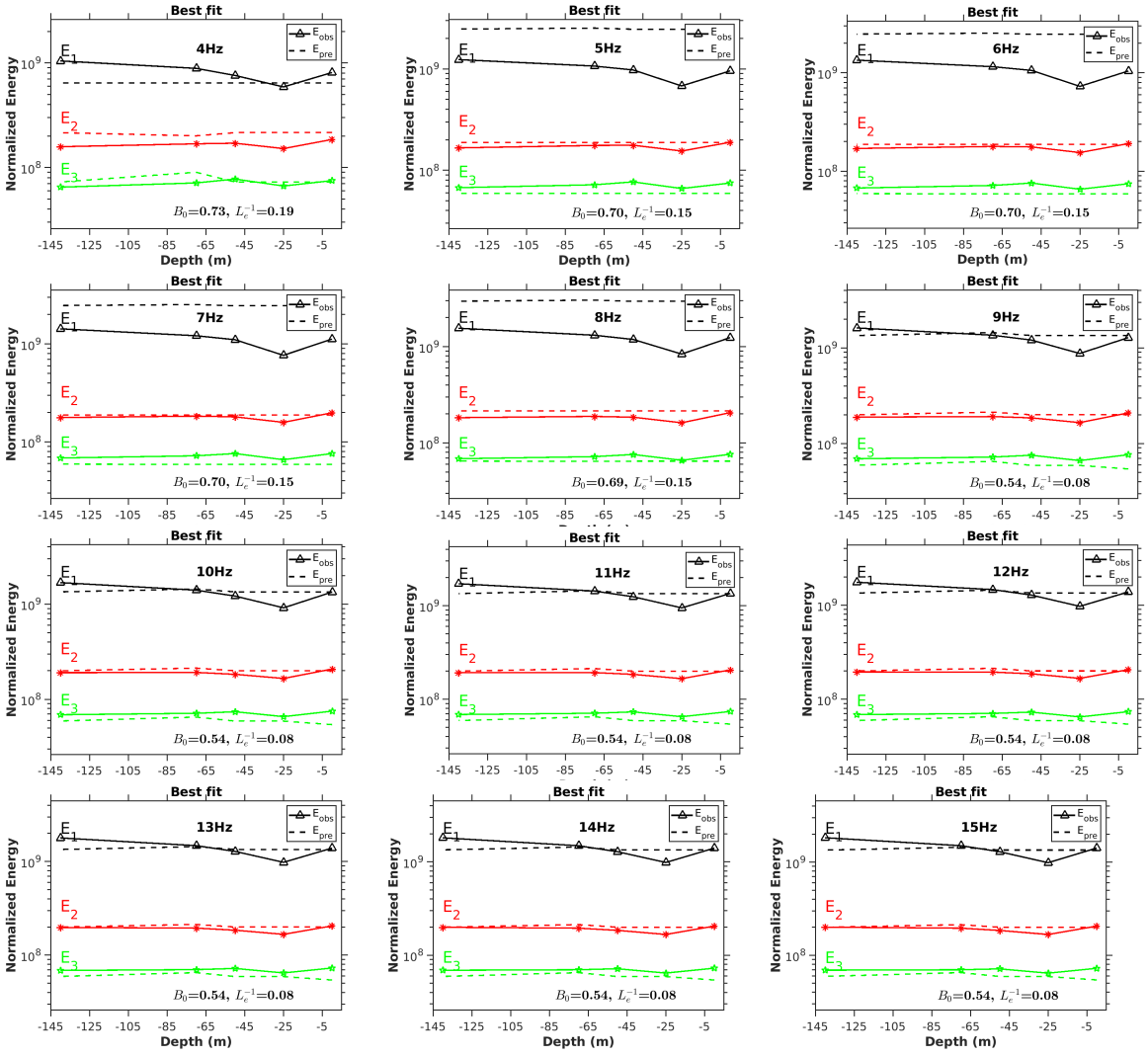

Figure C.1: Bestfit energy from borehole station